NI

NASA Technical Memorandum 83151

A TILE-GAP FLOW MODEL FOR USE IN AERODYNAMIC
LOADS ASSESSMENT OF SPACE SHUTTLE THERMAL
PROTECTIC'J SYSTEM: PARALLEL GAP FACES

Douglas L. Dwoyer, Perry A. Newman, Frank C.
Thames, and N. Duane Melson

OCTOBER 1981

TABLE OF CONTENTS

SUMMARY

The problem of predicting aerodynamic loads on the insulating tiles of the Space Shuttle Thermal Protection System (TPS) is discussed and seen to require a method for predicting pressure and mass flux in the gaps between tiles. A mathematical model of the tile-gap flow is developed based upon a slow viscous (Stokes) flow analysis and is verified against available experimental data. This model derives the tile-gap pressure field from a solution of the two-dimensional Laplace equation; the mass flux vector is then calculated from the pressure gradient. The means for incorporating this model into a lumped-parameter network analogy for porous-media flow is also given. The flow model shows tile-gap mass flux to be very sensitive to the gap width indicating a need for coupling the TPS flow and tile displacement calculations. Finally, recommendations are made concerning additional analytical and experimental work to improve TPS flow predictions and regarding a possible Shuttle TPS hardware modification.

INTRODUCTION

During the ascent of the Space Shuttle, the vehicle passes through subsonic, transonic, and supersonic speed regimes. Since the craft accelerates very quickly from the launch pad, the transonic regime is encountered at approximately 6,100 m (20,000 ft) where the atmosphere is still quite dense. This leads to a high dynamic pressure which, when coupled with the shocks present in

the transonic flow, produces large aerodynamic loads on the shuttle TPS tiles. Many of the tiles subjected to large localized loads were identified, removed, and replaced with stronger, "densified" tiles prior to STS-1 launch (ref. 1). However, the following questions remained: (1) Could densified tiles withstand the anticipated severe aerodynamic loads? and (2) Were all of the critically loaded tiles identified?

In response to question (1), wind-tunnel experiments were conducted on several different TPS test panels in order to measure forces and moments as well as pressures in, under, and around tiles. Generally, these panels were composed of "densified" tiles such as those subject to the severest shock-load conditions.

In response to question (2), continued tile loads assessment by the NASA Langley Structures Team (NLST), particularly for shocks impinging upon the TPS, indicated a questionable margin of safety for a number of as yet "undensified" tiles. A validation of the tile loads model as used by the NLST was performed utilizing the experimental data from the TPS panel tests, which indicated the need for a more accurate model.

As a result of these concerns, a more rigorous, independent tile shock-loads analysis was initiated by the NLST. Here, the flow through the porous tile, strain isolation pad (SIP), and filler bar, as well as in the gaps around the tile, was to be calculated in order to obtain the tile loads. Flow through the porous media (tile, SIP, and filler bar) was readily modeled in

the MITAS-II heat-transfer code (ref. 2). It was not immediately understood, however, how to model the flow through the tile gaps.

As a part of the NLST effort, the authors undertook the development of a model for the tile-gap flow. The results of the effort are presented in this paper. As will be shown, the model predicts that the flow in the tile gaps is strongly dependent upon the magnitude of the tile gap width; thus, calculations of aerodynamic loads on an individual tile cannot be uncoupled from its relative mo·ion in the TPS. Results and recommendations of this effort were available before the STS-1 launch.

Development of the present tile-gap flow model in a timely manner was enhanced by helpful discussions with and numerical solutions b: J. D. Keller and J. C. South, Jr. (Theoretical Aerodynamics Branch, Transonic Aerodynamics Division) and J. L. Thomas (Subsonic Aerodynamics Branch, Low-Speed Aerodynamics Division).

SYMBOLS

$\vec{A}$ vector streamfunction

D   tile-gap depth (cm)

d   distance measured along tile diagonal (cm)

f   velocity profile function

H $(h^+/h^-)^3$ where $h^+ + h^- = 2h_r$

h   tile-gap width (cm)

L   tile side length (cm)

M   Mach number

$\vec{\dot{M}}$ mass flux vector

$\dot{m}$ mass flow rate in x-direction per unit length

$\dot{n}$ mass flow rate in y-direction per unit length

p   pressure (kPa)

R   Reynolds number

R_r reduced Reynolds number

S_{ij} finite difference residual of Laplace equation for pressure

t   time (sec)

U,V   gap centerline velocity components in x- and y-directions, respectively (cm/sec)

u,v,w   velocity components in x-, y-, and z-directions, respectively (cm/sec)

U_∞ inviscid freestream velocity (cm/sec)

$\vec{V}$ velocity vector (cm/sec)

x,y,z   Cartesian coordinates defined in figure 2 (cr)

$\Delta x, \Delta y$ mesh increments in x- and y-directions, respectively (cm)

δ^* boundary-layer displacement thickness (cm)

μ coefficient of viscosity $\left(gm/(cm\text{-}sec) \right)$

ρ density (gm/cm^3)

σ conductance (cm-sec)

ϕ velocty potential function (cm^2/sec)

$\vec{\omega}$ vorticity vector (sec^{-1})

∇^2 Laplacian operator (cm^{-2})

∇_2^2 two-dimensional Laplacian operator (cm^{-2})

$[q]$ jump in q across discontinuity

4

Subscripts

I	number of mesh points in x-direction
i,j	mesh increment counters in x- and y-directions, respectively
r	reference conditions
t	differentiation with respect to time
x,y,z	differentiation with respect to indicated variable
∞	outer inviscid freestream conditions

Superscripts

*	dimensional quantity
'	differentiation with respect to argument
+	conditions downstream of discontinuity
-	conditions upstream of discontinuity

TILE-GAP FLOW MODEL

Schematic diagrams of the TPS component arrangement are shown in figure 1. The main components of the system are the porous ceramic tiles and the nomex felt strain isolation pad. The tiles have an impervious coating on all exposed surfaces with the exception of a small strip around the base called the terminator gap. The glue bonds between the tile and SIP are also considered impervious. The filler bars form a matrix on the aluminum skin of the shuttle into which individual tile/SIP assemblies are glued. Adjacent tiles are separated by a narrow gap of up to 0.13 cm (0.05 in). The filler bar is glued to the skin but neither to the tile nor SIP; thus, tile motion in response to aerodynamic

5

loads can lead to the opening of a small gap between the tile and filler bar (termed the filler bar gap).

The shuttle flow field at transonic flight conditions contains shock waves which may be located on particular tiles so that the pressure on the downstream portion of the tile is higher than the pressure on the upstream portion. Both the tile and SIP are porous, thus allowing a flow path for the high-pressure gas to develop in response to the tile-surface-pressure gradient. In such a situation, high-pressure air can move down the tile gap and into both the tile through the terminator gap at the bottom of the tile and the SIP through the filler-bar gap. Gas flow in both the tile and SIP can be treated as porous-medium flow. In order to develop a full-tile flow-field model, however, one must be able to analyze the flow through the tile-to-tile gap and the tile-to-filler bar gap.

Rationale for Model

Guidance in the development of a tile-gap flow model may be obtained from a Reynolds number estimate. At transonic ascent conditions there is a turbulent boundary layer on the tile outer surface so that, at the top of the narrow tile-to-tile gap, velocity components are very small. If one takes the normal velocity (V_r^*) induced by the turbulent boundary-layer growth along the sh·ttle surface as a measure of the gap velocity, then this velocity is approximately

6

$$V_r^* = U_\infty^* \left(\frac{d\delta^*}{dx^*}\right)_\infty = 0.037 U_\infty^* R_\infty^{-1/5} \tag{1}$$

For the STS-1 shuttle ascent trajectory, an appropriate transonic flight condition near maximum dynamic pressure is $M_\infty = 0.9$ at about 6,100-m (20,000-ft) altitude. The Reynolds number based on 1/2 mean chord is about 80 million. Using equation (1) then gives $V_r^* = 27.7$ cm/sec (0.91 ft/sec); i.e., very slow flow. Since both the tile gap to tile length $\frac{h^*}{L^*} \approx \frac{1}{120}$ and tile gap to tile depth $\frac{h^*}{D^*} \approx \frac{1}{50}$ are very small for most tiles, one would expect the "slow creeping flow" approximation to be valid. According to reference 3, the appropriate Reynolds number for very slow flows (such as Stokes flow, lubrication theory flow, Hele-Shaw flow) is a reduced Reynolds number given by an expression of the form

$$R_r = \frac{\rho_r^* V_r^* L^*}{\mu_r^*} \left(\frac{h^*}{L^*}\right)^2 \tag{2}$$

Substituting the previously given parameters in equation (2) yields a reduced Reynolds number for the gap flow of $R_r = 0.12$. Since many of the very slow flow models are reasonably valid up to $R_r = 4$ or 5, a model of this type is utilized for the tile-gap flow.

Governing Equations

The basic approximation in creeping flow is that the fluid is incompressible and that the viscous forces dominate the convective

7

forces. Therefore, if the convective forces are neglected, the incompressible Navier-Stokes equations reduce to

$$\nabla^2 p = 0 \tag{3}$$

$$\vec{V}_t + \vec{\nabla}p = R^{-1}\nabla^2\vec{V} \tag{4}$$

where all quantities have been normalized according to the following scheme

$$\vec{V} = \frac{\vec{V}^*}{V_r^*}, \quad \vec{\nabla} = h^*\vec{\nabla}^*, \quad t = \frac{t^* V_r^*}{h^*}, \quad p = \frac{p^*}{\rho_r^* V_r^{*2}} \tag{5}$$

with

$$R = \frac{\rho_r^* V_r^* h^*}{\mu_r^*} = R_r \frac{L^*}{h^*}$$

The coordinate system is defined in figure 2.

Recalling that the tile gaps are quite deep yet very narrow, and assuming that their faces remain parallel, we then take the velocity component across the gap to be small compared to the other two components (i.e., assume $w \approx 0$). Therefore, the z-component of the momentum equation (eq. 4) reduces to

$$\frac{\partial p}{\partial z} = 0$$

which upon integration yields

$$p = p(x,y) \tag{6}$$

8

The final assumption in the flow model is that the solutions for u and v are separable. That is,

$$\left. \begin{array}{l} u(x,y,z) = f(z)\ U(x,y) \\ v(x,y,z) = f(z)\ V(x,y) \end{array} \right\} \tag{7}$$

It is easily verified that the function $f(z)$ must be the same for both u and v if the velocity vector is to remain divergence free. Substitution of equations (6) and (7) into equations (3) and (4) gives (for steady flow)

$$\nabla_2^2 p = 0 \tag{8}$$

$$p_x = R^{-1} f \nabla_2^2 U + R^{-1} f'' U \tag{9}$$

and

$$p_y = R^{-1} f \nabla_2^2 V + R^{-1} f'' V \tag{10}$$

The no-slip boundary condition at the gap walls requires that f vanish there. Normalization of f at the center of the gap then yields

$$\left. \begin{array}{l} f(0) = 0 \\ f(1) = 0 \\ f(0.5) = 1 \end{array} \right\} \tag{11}$$

Since U and V are independent of z and equations (9) and (10) are valid for any value of z, we evaluate these equations at z = 0 and obtain

$$U = \frac{Rp_x}{f''(0)}$$

$$V = \frac{Rp_y}{f''(0)}$$

Direct calculation of $\nabla_2^2 U$ and $\nabla_2^2 V$ gives (in view of eq. (8))

$$\left.\begin{array}{l} \nabla_2^2 U = \dfrac{R}{f''(0)} \dfrac{\partial}{\partial x} \nabla_2^2 p = 0 \\[3em] \nabla_2^2 V = \dfrac{R}{f''(0)} \dfrac{\partial}{\partial y} \nabla_2^2 p = 0 \end{array}\right\} \tag{12}$$

It thus follows from equations (6), (9), (10), and (12) that

$$f''(z) = \text{constant} \tag{1}$$

The profile function $f(z)$ satisfying equations (11) and (13) is then

$$f(z) = -4z(z-1) \tag{14}$$

Expressions for U and V which follow from equations (8), (10), (12), and (14) are

$$\left.\begin{array}{l} U = -Rp_x/8 \\[2em] V = -Rp_y/8 \end{array}\right\} \tag{15}$$

10

In appendix A, a derivation of these results is given in terms of velocity vector potential functions.

It may be observed from equation (8) that the solution for the pressure field in the gap is decoupled from the solution of the velocity field if the pressure boundary conditions are independent of the gap velocities. For such cases, the pressure field is obtained as a solution of equation (8) and the velocity field is then obtained from equations (7), (14), and (15).

Pressure Boundary Conditions

In order to solve equation (8) for the pressure field in the tile gaps, boundary conditions are required. We assume that the pressure distribution at the top of the gap is known, since the pressure over the entire tile outer surface is established by the large-scale flow field of the shuttle itself and "drives" the TPS flow. At the bottom of the gap, two types of boundary conditions were considered. First, in order to validate the flow model, initial comparisons with experimental data used pressures spe·fied along the gap bottom; that is, Dirichlet boundary conditions. Second, in calculations which might be interacted with a porous-medium code for the internal tile and SIP flows, the vertical mass-flow rate per unit length would be specified. It will be seen that this specification required that p_y be given along the gap bottom; that is, Neumann boundary conditions. Similarly, along the vertical boundaries of a tile face a mass-flux condition can be used to form an interface boundary condition

11

from the solution for the adjoining tile faces. This procedure will be described in more detail subsequently.

Mass Flow Rates

The mass-flow rate per unit length of gap in either the x- or y-direction can be readily calculated from the previous equations. For example, the mass-flow rate in the x-direction is given by

$$\dot{m} = \int_0^1 u \, dz$$

which becomes, upon using equations (7), (14), and (15)

$$\dot{m} = -Rp_x/12 \tag{16}$$

A similar integration yields for the y-direction flux

$$\dot{n} = -Rp_y/12 \tag{17}$$

Dimensional forms of equations (16) and (17) are

$$\left. \begin{aligned} \dot{m}^* &= -\frac{\rho_r^* h^{*3}}{12\mu_r^*} \frac{\partial p^*}{\partial x^*} \\[2ex] \dot{n}^* &= -\frac{\rho_r^* h^{*3}}{12\mu_r^*} \frac{\partial p^*}{\partial y^*} \end{aligned} \right\} \tag{18}$$

Equations (18) indicate that the dimensional mass-flow rate through the narrow gap is proportional to the product of the cube

12

of the gap width and the pressure gradient. Thus, the mass flux through the tile gap will be quite sensitive to changes in the gap width. Thus, in making aerodynamic loads assessments for the TPS, one must couple the TPS flow calculations with the tile motion due to aerodynamic and other forces in those regions where relative tile motions can occur.

TILE-GAP FLOW/TILE DISPLACEMENT COUPLING

The large relative tile motions observed during the Combined Loads Orbiter Test (CLOT) series conducted in the NASA Langley 8-Foot Transonic Pressure Tunnel appear to have occurred in the vicinity of shock waves. The observed tile chipping indicates that in some places the tile gaps were essentially closed at times. Thus, one suspects that, in the region of shocks, some of the tile gaps effectively close causing high pressures under adjacent tiles.

Flow Metering by Variable Gap Width

The coefficient of the pressure gradient in an equation like equation (18) is, in effect, the "porosity" (conductance or reciprocal resistance) of the medium which, in this case, is the gap itself. The size of this "porosity" is essentially determined by the gap width, h. When several porous elements are connected together (such as the tile gaps, SIP, filler bars, and porous tile, as shown in fig. 1), the resulting mass flow is governed by effective porosities as seen locally within the network. In a

series circuit, the smallest porosity meters the flow and sustains the largest pressure gradient; whereas, in a parallel circuit, the bulk of the flow passes through the most porous branch with essentially no flow through the less porous branches. The TPS flowfield can be modeled as a complex network containing many series and parallel connections. As a tile gap narrows, it will effectively meter the flow when its porosity becomes smaller than that of the other elements. That is, there will be little flow through it; or, conversely, it will support a large pressure gradient.

The relative magnitude of porosity for all of the elements involved in the network needs to be known or amenable to calculation for a valid prediction of the flow. As already indicated, the porosity of the tile gap depends upon the gap width which changes with relative tile motion. Some measurements of the nominal tile and SIP material porosities have been made (ref. 4). The tile itself is rigid enough so that its porosity is probably unaffected by tile block dynamics. However, the porosity of the spongy, felt-like SIP material should change with the tile block motions and other loads which are superimposed upon it. Using the data of reference 4, an estimate is made of the SIP porosity for dimensions appropriate to this study in appendix B and this value was used to normalize the coefficient σ^* for the variable tile gap which is presented in figure 3. The value for the SIP porosity used in the normalization should be considered a lower bound, since flow through the sample in the experiment of reference 4 was conducted with atmospheric pressure superimposed on the

14

large SIP faces. Under flight conditions where one is concerned
with tiles at and just ahead of a shock wave, the tile block will
be tending to lift and the SIP will be under tension (stretched
or fluffed up) and will become more porous. The point is, at
some reasonable, narrow, tile-gap width, the "porosity" of the
gap becomes smaller than that of the SIP. When no constraining
devices have been inserted between the tiles, the minimum tile-
gap width will be determined by the surface roughness, waviness,
or curvature of the individual adjacent tile faces.

If one is depending upon the nominal gap widths on all sides
of a tile block to relieve pressure gradients between the tile
upper surface and the SIP, then a lateral shift of the tile will
result in differential relieving effects. Furthermore, flow under
a given shifted tile may find the path of least resistance to be
under an adjacent tile rather than to the upper surface through a
very narrow tile gap. Around shock waves, such lateral tile dis-
placements are expected.

Lateral Tile Displacement Due to Shock Load

Since the tiles are not directly mounted on a rigid surface,
but rather to the nonrigid SIP, lateral tile displacements due to
shock pressure loads alone can be large enough to close the tile
gap. This can be seen by considering typical shuttle flow condi-
tions and measured SIP properties.

An estimate of the side or shearing load on a tile is made by
assuming a normal shock impinging across the middle of a tile

oriented as in figure 1. At M_∞ = 0.9, it is not unreasonable to
assume a local Mach number of 1.2 ahead of the shock. At an
altitude of 6,100 m (20,000 ft), a 15.24-cm × 15.24-cm × 6.35-cm
(6-in × 6-in × 2.5-in) tile develops an upstream force of 133 N
(30 lbf) if it is assumed that the pressure in all of the gaps is
constant in the y-direction. This yields a shear stress in the
SIP of 8.41 kPa (1.22 psi) if one assumes a 161-cm^2 (25-in^2) SIP.

In figure 4, experimentally determined stress-strain proper-
ties of the SIP loaded in shear (ref. 5) are presented. From the
figure, it is seen that a shear stress on the order of 6.89 kPa
(1 psi) should move the tile 0.23 cm (0.09 in), an amount more
than sufficient to close the tile gap (nominally 0.13 cm (0.05 in))
on the low pressure (upstream) side of the tile (assuming adjacent
tiles remain fixed). The model for the TPS flow field must, there-
fore, be coupled with the structural dynamics of the TPS in order
to accu_ately predict tile aerodynamic loads.

APPLICATION TO TPS GEOMETRY

In order to assess the validity of the proposed gap-flow
model, on first considers flow about a single tile. The situa-
tion 'u somewhat different than shown in figure 1, in that the
si_ngle tile is surrounded by a solid wall. The tile is, however,
allowed to move laterally so that the tile-gap width may not be
ui_iform around the tile. Two equivalent solution algorithms are
discu_sed in the following sections. One can solve a number of
coupled Laplace equations, such as equation (8), for flow in the

16

tile gaps as well as in the truly porous material (i.e., the tile, SIP, and filler bars); or one can solve a lumped-parameter network representation of diffusion equations, such as equations (18), in the tile gaps, again with analogous equations for the truly porous media. Both approaches are discussed here, since the former was used to quickly determine that the present tile-gap flow model was reasonable while the latter is being used by the NLST in full TPS assessments.

Laplace Equation Solver

It is expected that the creeping flow model will not be strictly applicable in a small vicinity about the tile edges. However, for the purposes of simplicity, all of the edge regions are treated here using the same model. Keeping this assumption in mind, the gap around the tile (fig. 5) can be "unwrapped" into a flat solution space. Equation (8) is to be solved for the pressure field in the flat space. Since the gap facing each of the four sides of the tile can have a different width, a special interface condition must be applied along the vertical edges in figure 5. This interface condition is obtained by requiring mass conservation across each interface line.

From equation (18) it can be seen that, if $\dot{m}^*$ is to be continuous across an interface boundary, then $\partial p^*/\partial x^*$ cannot be continuous if the gap width, h^*, is discontinuous there. However, the pressure, p^*, must be continuous across the interface boundary. Equation (18), evaluated on either side of the interface, is then

$$(\dot{m}^*)^- = \frac{-\rho_r^* \left[(h^*)^-\right]^3}{12\mu_r^*} \left(\frac{\partial p^*}{\partial x^*}\right)^-$$

and

$$(\dot{m}^*)^+ = \frac{-\rho_r^* \left[(h^*)^+\right]^3}{12\mu_r^*} \left(\frac{\partial p^*}{\partial x^*}\right)^+$$

Thus, if $(\dot{m}^*)^- = (\dot{m}^*)^+$ one obtains

$$\left.\begin{aligned}
\left(\frac{\partial p^*}{\partial x^*}\right)^- &= H \left(\frac{\partial p^*}{\partial x^*}\right)^+ \\[2em]
\text{where} \quad H &= \left(\frac{h^+}{h^-}\right)^3
\end{aligned}\right\} \tag{19}$$

Also, as stated before

$$(p^*)^- = (p^*)^+ \tag{20}$$

The isolated tile-gap solution procedure is to solve equation (8) with $p^\bullet$ specified along the top of the gap and either p^* or $\partial p^*/\partial y^*$ specified along the bottom of the gap. In the most general case, four interface conditions of the type given by equations (19) and (20) must also be satisfied. For the cases

18

calculated in the present report, symmetry was assumed along the tile diagonal alined with the outer inviscid flow; thus, only one value of H appears when the tile is displaced along this diagonal. In order to compute the distribution of p^* in the gaps, a second-order accurate finite-difference analog of equation (8) was solved using a successive line over-relaxation (SLOR) procedure (ref. 6). The details of this well-known procedure will not be given here; some comments on how the interface condition was implemented are appropriate and are given in appendix C.

For a single-tile experiment, where only that one tile can move, the gap widths are constrained. That is, the average of gap widths on opposite tile faces are related by

$$(h^*)^- + (h^*)^+ = 2h_r^* \qquad (21)$$

Upon using the definition of H (eq. (19)) one obtains from equation (21)

$$\left. \begin{array}{c} \dfrac{(h^*)^+}{h_r^*} = \dfrac{2H^{1/3}}{H^{1/3} + 1} \\[2em] \text{and} \\[2em] \dfrac{(h^*)^-}{h_r^*} = \dfrac{2}{H^{1/3} + 1} \end{array} \right\} \qquad (22)$$

Diffusion Equation Solver

The MITAS-II (ref. 2) computer program is designed to solve problems governed by diffusion-type equations using a lumped-parameter network representation. The resulting system of equations is solved using a point relaxation scheme, which by current standards is not computationally efficient but is quite reliable. This program is well suited to solving the flow in truly porous media, such as the flow inside the tile and SIP materials. In order to solve fluid-flow problems using this technique, a resistance law must be provided in the form

$$\dot{\vec{M}}^* = \sigma^* \vec{\nabla}^* p^*$$ (23)

where $\sigma^* = \sigma^*(x^*,y^*,z^*)$ is a conductance or porosity. For the model of the tile-gap flow field derived in the present work, one may readily identify σ^* from equation (18) as

$$\sigma^* = \frac{-\rho_r^* h^{*3}}{12\mu_r^*}$$ (24)

and, thus, easily include the tile-gap flow model into the network analysis.

Incorporation of the tile-gap flow model of equations (23) and (24) into the diffusion network, allows one to solve the entire TPS flow field simultaneously by utilizing only the MITAS-II program. Since one expects the gap width h^* (and, thus, σ^*) to

20

vary due to pressure loads and SIP mechanical response, as discussed above, one must include such structural response characteristics in an entire TPS analysis. Furthermore, this structural response must be iteratively interacted with the diffusion network solver since the changing gap width h^* will strongly affect the mass-flow rates. This interaction will be required not only for a time-dependent (dynamical) analysis; but, also, for the mean-steady flow to reach an equilibrium state which is what is envisioned here.

COMPARISON WITH EXPERIMENTAL DATA

Results calculated using the present model for tile-gap flow are here compared with unpublished experimental data from two tests. The first compares Laplace solver results with those from the OS-52 test conducted at the NASA Ames Research Center (ARC). In this comparison, the tile-gap flow solution obtained using experimental boundary data and no interaction with the porous tile or SIP is compared with measured results in order to test the validity of the creeping flow assumption. The second compares single-tile-network results with those from the simulated shock test conducted at the NASA Johnson Space Center (JSC). The theoretical prediction was made using the MITAS-II computer program with all of the TPS components modeled. This calculation was made by Dr. George Ivey and Mr. Dennis Petley of the Systems Engineering Division of NASA Langley Research Center (LaRC).

Comparison With NASA OS-52 Test

In the OS-52 test, a panel of tiles was subjected to an aerodynamic loading in a transonic wind tunnel which simulated flight ascent conditions. A schematic diagram of the test arrangement is shown in figure 6. In this experiment, the test tile with its associated gaps and SIP was instrumented for pressure measurements, detailed enough for attempting a gap-flow model assessment. Pressures were measured along vertical columns down the gaps at the eight locations indicated in figure 7. Figure 7 also shows a cross-section of the instrumented test and adjacent dummy tiles indicating the location of the gap pressure taps and the particular TPS arrangement for this test. Note that only the test tile is mounted on the SIP and that the aluminum wall is breached around the entire SIP base to allow a direct tile load measurement. The entire TPS flow field is open to a plenum beneath the aluminum wall. This arrangement compromises the fidelity of the experiment, in that flow through the porous tile and SIP are short-circuited. However, for the purposes of this study, the detailed gap pressure measurements allow a direct assessment of the adequacy of a creeping flow assumption for the gap-flow model.

In the present comparison, equation (8) was solved for the pressure distribution in the gap around the entire test tile with the tile in its nominal centered position. The pressure specified as the boundary data along both the top and bottom of the gap was taken from the measured experimental data. The flow field was assumed to be symmetric about the tile diagonal alined with the

flow direction, since measured data were taken on only two tile

sides as indicated in figure 7. Comparisons of the predicted

and measured pressure distributions for six runs from the OS-52

test series are shown in figure 8. These six runs represent cases

where an undensified tile was subjected to a shock load, with

relevant experimental conditions summarized in table I. Compari-

son in all six cases is seen to be excellent. This result is

interpreted to mean that the pressure in the narrow tile gap is

interpolated by Laplace's equation. From the Navier-Stokes equa-

tions one sees that, if inertial forces are comparable to the

pressure and viscous forces, then the Laplacian of pressure would

not vanish and one would expect discrepancies to appear in compari-

sons such as those presented in figure 8. This result is taken as

evidence in support of the validity of the creeping flow assumption

for the gap flow model.

The effect of tile displacement on details of the calculated

pressure distribution in the gaps for OS-52 test run 31:4 is shown

in figure 9. The same experimental pressures were used as

Dirichlet boundary data at both the top and bottom of the tile

gap. It is seen that the pressure distribution is altered only

in the immediate vicinity of the corner. In the pressure compari-

sons of figure 8, the effect of changing H (that is, shifting

the tile) cannot be detected to the accuracy of the plots.

As would be expected from equations (18), the effect of tile

displacement on the mass flux in the gaps is large. Calculated

mass-flux vector plots for OS-52 test run 31:4 are shown in

23

figure 10 for various tile displacements from the nominal position. After the front gaps have closed about halfway (i.e., H = 27), the mass flux through them has virtually disappeared. Further tile displacement appears to have little effect on the mass flux. The expected strong metering ability of varying tile-gap width is thus demonstrated numerically. Since neither gap-flow velocities nor mass flux measurements were made in the OS-52 tes' comparison with experiment is not possible for these quantit.

Comparison With NASA JSC Simulated Shock Test

The JSC simulated shock test was a static-tile, shock-load simulation. In this test, a single tile was mounted on the SIP and was placed in a pressure vessel divided by a bulkhead as shown schematically in figure 11. Different pressures were maintained in the two chambers of the vessel and the only communication path between them was the TPS flow field. Pressures were measured in the SIP and at the tile bond line (TBL) at the pressure taps shown in figure 11.

The MITAS-II computer program was used to calculate the TPS flow field for this test arrangement; that is, a single-tile network. Equations (18) were used to model the tile-gap flow, with the porosity given by equation (24), while the porosities for the SIP and tile were taken from the data of reference 4.

In the JSC test, the tile was held fixed with r·spect to the bulkhead with nominal gap widths of 0.11 cm (0.045 in). Two comparisons of measured and predicted pressure distributions along

24

the tile diagonal denoted d^*_{TBL} at the TBL are shown in figure 12; the pressure jump, $\left|p\right|$ = 17.9 kPa (2.6 psia), simulate a shock wave occurring on the tile outer surface. The simu ...ed shock is located at about 33 percent of the distance along the tile dia₀nal in figure 12(a) and at about 61 percent in figure 12(b). For both cases, the predicted and measured pressure at the TBL agree to about 0.69 kPa (0.1 psia), which is considered to be very good. Similar agreement was obtained for the SIP pressures.

One concludes from both the experimental and computed results that the flow is being metered by the SIP and/or tile. Thus, the porosity of the SIP and/or tile is less than the effective porosity of the tile gaps of nominal width. Calculations were also made for the tile slightly displaced, simulating the change in gap widths due to shock loads. These numerically demonstrate not only the mass-flow changes as previously shown in figure 10, but also the changes in pressure level and gradient locations when the narrow tile gaps (on the low-pressure side of the shock) meter the TPS flow. Unfortunately, the JSC test was not successful in obtaining pressure data for the test tile slightly shifted so that comparisons could be made. Such tests are still deemed to be important in validating the present flow model.

CONCLUDING REMARKS

The present study allows one to draw several conclusions about the TPS flow field. Calculations made in conjunction with the OS-52 test data indicate that the flow in the tile gaps is

governed by the creeping or slow viscous flow equations. The
remaining elements of the TPS; i.e., the tile, SIP, and filler
bar are truly porous media wherein fluid flow is governed by the
same equations (ref. 3). Thus, the entire TPS flow field can be
treated as a slow viscous flow where local values of porosity
depend not only upon the medium but also upon the loads and tile
displacement.

The derivation presented here identifies a potentially strong
flow-metering mechanism due to a change in the tile-gap width.
The mass-flow rate through the tile gap is linearly proportional
to the pressure gradient, but proportional to the cube of the gap
width. Thus, the mass-flow rate through the gaps is extremely
sensitive to tile displacement and motion. This fact provides a
rational mechrnism for explaining the experimentally observed high
ᵥIP pressures in the vicinity of a shock wave. Shock-pressure loads
force the tile upstream toward its neighbor, thus reducing the gap
width on the low-pressure side. This narrowed gap then becomes
the most resistive element in the flow field around a given tile
and, hence, experiences the major part of the pressure drop.

Another remark should be made about the tile displacements
considered in this report. Only lateral displacements in a direc-
tion parallel to the outer flow were considered here. In general,
the tile motion has 6 degrees of freedom and is constrained in its
response to pressure and skin-friction loads by adjacent tiles and
SIP. Such motion will, in general, create gaps whose sides are
not parallel. Given the sensitivity of mass-flow rate to gap

26

width, one can expect to have strong local metering in such cases. Accounting for such general tile motions by calculating suitable average gap widths will probably not reflect this strong local metering. Preliminary conclusions drawn in comparing calculated results from the MITAS-II computer program with those from the JSC simulated shock test indicate, however, that the nominal SIP porosity is lower than the nominal effective tile-gap porosity for that test. In order that the MITAS-II program accurately predict TPS flow fields, one must include a model of the effect of SIP deformation on SIP porosity. This is necessary in order to identify the crossover point where the tile gap becomes less conductive than the SIP under load. Sufficient experimental data to develop and verify such a model is not available at this writing.

In view of the uncertainty in some of the very basic parameters involved in this TPS flow-field model, the complexity of the entire shuttle TPS and the wide range of aerodynamic conditions to which it is exposed during a typical mission, great care should be exercised in interpreting predictions made by this model. In particular, if predictions of tile loads made by this TPS flow-field analysis are to be used in assessing hardware safety margins, then every effort should be made to eliminate uncertainties in the basic physical parameters used in the calculations as well as further model verifications. In this regard, specific recommendations are made in the next section.

RECOMMENDATIONS

Results of the current study indicate a need for work in several areas to improve the analytical prediction capability for aerodynamic loads assessment of the shuttle TPS. Specific recommendations are:

(1) Make further measurements of the SIP material porosity, particularly under the structural loading conditions appropriate to shuttle flows with shock waves.

(2) Conduct single-tile simulated shock tests (similar to the JSC simulated shock test) allowing for arbitrary gap widths which are not necessarily parallel.

(3) Extend the current analysis to the case of nonparallel gap faces.

(4) Enhance the computational efficiency of the MITAS-II program by making the code operational on the CYBER 203 system with a faster solution algorithm.

These recommendations were made to the NLST and action has been initiated on items (1)-(3).

In regard to the actual shuttle TPS hardware, it is strongly suggested that consideration be given to finding and making a simple modification to restrain an individual tile's relative displacement so as to nearly maintain the nominal effective tile-gap porosity.

REFERENCES

1. Cooper, Paul A.; and Holloway, Paul F.: The Shuttle Tile Story. Astronautics and Aeronautics, pp. 24-36, Jan. 198.

2. Anon: MITAS-II, Martin-Marietta Interactive Thermal Analysis System Version-2.0. User's Manual. Martin-Marietta Report M-76-2, May 1976.

3. Schlicting, Herman: Boundary Layer Theory. Fourth Edition. McGraw-Hill Book Co, Inc., New York, NY, 1960.

4. Lawing, Pierce L.; and Nystrom, Donna M.: Pressure Drop Characteristics for Shuttle Orbiter Thermal Protection System Components; High Density Tile, Low Density Tile, Densified Low Density Tile and Strain Isolation Pad. NASA TM 81891, Oct. 1980.

5. Sawyer, James Wayne; and Waters, William Allen, Jr.: Room Temperature Shear Properties of the Strain Isolation Pad for the Shuttle Thermal Protection System. NASA TM 81900, Jan. 1981.

6. Roache, Patrick J.: Computational Fluid Dynamics. Hermosa Publishers, Albuquerque, NM, 1972.

APPENDIX A

DERIVATION OF THE TILE-GAP-FLOW EQUATIONS USING VELOCITY
VECTOR POTENTIAL FUNCTIONS

Derivation of the governing tile-gap-flow equations for the case of parallel gap faces by utilizing vector potential functions gives insight into how a separation of variables should be attempt ed and hopefully how the more general case of nonparallel gap faces might be approached. The appropriate steady Navier-Stokes equation (from eq. (4)) is

$$R\vec{\nabla}p = \nabla^2\vec{V} \tag{A1}$$

where the flow is incompressible

$$\vec{\nabla} \cdot \vec{V} = 0 \tag{A2}$$

with no slip on the gap faces $(z = z_f)$

$$\left.\begin{array}{l} V(x,y,z_f) = 0 \\ z_f = 0,1 \end{array}\right\} \tag{A3}$$

and no flow across the gap

$$w = 0 \tag{A4}$$

It appears that there are three scalar quantities in the above for which one must obtain a consistent separation of variables; that

is, p and the two nonzero components of $\vec{V}$. Introduction of a velocity vector potential function from which all three of these scalar quantities can be derived aids in the separation. In order to proceed, one needs to recall a vector identity

$$\nabla^2\vec{V} = \vec{\nabla}(\vec{\nabla} \cdot \vec{V}) - \vec{\nabla} \times \vec{\nabla} \times \vec{V} \tag{A5}$$

and the general vector properties that a vector can be decomposed as

$$\vec{V} = \vec{\nabla}\phi + \vec{\nabla} \times \vec{A} \tag{A6}$$

and that

$$\left. \begin{array}{l} \vec{\nabla} \times \vec{\nabla}g \equiv 0, \quad g \quad \text{a scalar function} \\[2mm] \vec{\nabla} \cdot \vec{\nabla} \times \vec{B} \equiv 0, \quad \vec{B} \quad \text{a vector function} \end{array} \right\} \tag{A7}$$

Several general results follow directly from equations (A1), (A2), and (A5)-(A7):

$$\vec{\nabla} \cdot \vec{V} = 0 \qquad \nabla^2\phi = 0 \tag{A8}$$

$$R\vec{\nabla}p = - \vec{\nabla} \times \vec{\nabla} \times \vec{\nabla} \times \vec{A} \tag{A9}$$

$$\nabla^2 p = 0 \tag{A10}$$

From these equations, it is seen that the scalar potential function ϕ does not enter into constructing the solution for $\vec{\nabla}p$

31

whereas the vector potential $\vec{A}$ does. Note, however, that ϕ may be needed in order to satisfy no-slip velocity boundary conditions, such as equations (A3) and (A4), and that permissible $\phi(x,y,z)$ must satisfy Laplace's equation. One splits the vector potential $\vec{A}$ as

$$\vec{A} = \vec{A}_h + \vec{A}_p \tag{A11}$$

where A_h and A_p satisfy, respectively, the homogeneous and nonhomogeneous equations

$$\left.\begin{array}{l} \vec{\nabla} \times \vec{\nabla} \times \vec{\nabla} \times \vec{A}_h = 0 \\[2em] \vec{\nabla} \times \vec{\nabla} \times \vec{\nabla} \times \vec{A}_p = - R\vec{\nabla}p \end{array}\right\} \tag{A12}$$

The potential functions $\vec{A}_h$ and $\vec{A}_p$ are determined by satisfying the equations which result from taking the curl of equation (A12); that is,

$$\vec{\nabla} \times (-R\vec{\nabla}p) \equiv 0 = \vec{\nabla} \times \vec{\nabla} \times \vec{\nabla} \times \vec{\nabla} \times \vec{A} \tag{A13}$$

plus no-slip velocity conditions at all surfaces, such as equations (A3), and prescribed or imposed conditions on velocity or pressure, such as equations (A4) on w and (A12) on $\vec{\nabla}p$, at the gap edges.

For the fluid velocity vector $\vec{V}$, the vector potential $\vec{A}$ is the streamfunction. One introduces the vorticity, $\vec{\omega}$,

32

$$\vec{\omega} = 1/2 \; \vec{\nabla} \times \vec{V} = 1/2 \; \vec{\nabla} \times \vec{\nabla} \times \vec{A} \qquad \text{(A14)}$$

and it follows from equation (A13) that

$$\nabla^2 \vec{\omega} = 0 \qquad \text{(A15)}$$

The results of the two preceding paragraphs are general for slow creeping flow. To solve a specific boundary-value problem, appropriate boundary and symmetry conditions are satisfied by specializing the potential functions ϕ, $\vec{A}_h$, and $\vec{A}_p$. It is not our aim here to match or fit analytical solutions to arbitrary boundary conditions on p or $\vec{\nabla}p$ at the gap edges. Instead, we separate out the gap-normal coordinate dependence to obtain an equivalent 2-D problem in order to verify the gap-flow model and, thus, provide an engineering approximation for the NLST to use in tile loads assessment codes.

The condition (A4) is satisfied by

$$\vec{A} = \psi\hat{k} = (\Omega - \Pi) \; \hat{k} \qquad \text{(A16)}$$

where ψ is split into Ω satisfying the homogeneous equation (A12) while Π, the particular solution, satisfied the non-homogeneous equation (A12). Thus, the first of equations (A12) becomes

$$\vec{\nabla} \times \vec{\nabla} \times \vec{\nabla} \times \Omega\hat{k} = 0 \qquad \text{(A17)}$$

and it can be seen, for example, that any Ω for which

$$\nabla^2 \Omega = 0$$

33

is a solution of (A17). For the particular solution Π, one assumes a separation of variables

$$\Pi\ (x,y,z)\ =\ X(x)Y(y)Z(z) \tag{A18}$$

and determines these functions by simultaneously satisfying two vector equations (A13) and (A3) subject to the nonvanishing of the second equation (A12). Substitution of equations (A6) through (A18) into equation (A13) gives

$$\left.\begin{array}{l} 0 = \dfrac{\partial}{\partial x}\ \nabla^2(XYZ')\ =\ \dfrac{\partial}{\partial x}\ \left[\nabla_2^2(XYZ')\ +\ XYZ'''\right] \\[2em] 0 = \dfrac{\partial}{\partial y}\ \nabla^2(XYZ')\ =\ \dfrac{\partial}{\partial y}\ \left[\nabla_2^2(XYZ')\ +\ XYZ'''\right] \\[2em] 0 = \nabla^2\ \left[\nabla_2^2(XYZ)\right] \end{array}\right\} \tag{A19}$$

and into equations (A12) gives

$$\left.\begin{array}{l} Rp_x = \dfrac{\partial}{\partial y}\ \nabla^2(XYZ)\ =\ \dfrac{\partial}{\partial y}\ \left[\nabla_2^2(XYZ)\ +\ XYZ''\right]\ \neq\ g(z)\ \text{or}\ 0 \\[2em] Rp_y = -\dfrac{\partial}{\partial x}\ \nabla^2(XYZ)\ =\ -\dfrac{\partial}{\partial x}\ \left[\nabla_2^2(XYZ)\ +\ XYZ''\right]\ \neq\ g(z)\ \text{or}\ 0 \end{array}\right\} \tag{A20}$$

The parabolic profile

$$Z\ =\ Kz(z-1) \tag{A21}$$

is seen to simultaneously sati..fy equations (A19) and (A20) if

34

$$\nabla_2^2 (XY) = 0 \tag{A22}$$

where K is an arbitrary constant, set by normalizing the profile. It then follows that the particular solution

$$\Pi(x,y,z) = KX(x)Y(y)z(z-1) \tag{A23}$$

gives

$$
\left.
\begin{aligned}
u &= -KXY'z(z-1) \\
v &= KX'Yz(z-1) \\
w &\equiv 0 \\
Rp_x &= 2KXY' \\
Rp_y &= -2KX'Y \\
Rp_z &\equiv 0
\end{aligned}
\right\} \tag{A24}
$$

and

$$\nabla_2^2 p = 0 \tag{A25}$$

This is the desired consistent separation of the z-dependence with complete sets of functions $X(x)$ and $Y(y)$ to satisfy the imposed pressure or pressure gradient boundary conditions at the gap edges. These results are consistent with those derived differently in the text.

APPENDIX B

COMPARISON OF SIP AND GAP POROSITIES

The coefficient σ^* defined by equation (24) is the gap porosity (or conductance) per unit length normal to the flow direction. Customarily, one defines the coefficient per unit area, with that area being normal to the flux direction. However, in order to explicitly exhibit the entire dependence of mass flux upon the variable gap width, h^*, we have multiplied the conventional coefficient per unit area by the gap width. The analogous coefficient for the SIP is then the conventional coefficient per unit area times the SIP thickness. Comparison of the relative porosities of gap and SIP is made using the present gap model (eq. (24)) and the SIP data from reference 4, respectively.

The only SIP porosity data which we are aware of are given on figure 5 of reference 4. There, pressure drop data are plotted versus the measured volume flow rates per unit normal area. These data are nearly linear, so we may fit the data with a relation of the form:

$$\Delta p^* = S^* \left(\frac{\dot{v}^*}{A_n^*} \right) \tag{B1}$$

where Δp^* is the pressure drop, S^* is the fitted slope, $\dot{v}^*$ is the volume flow rate, and A_n^* is the area normal to the flux. For the experiment of reference 4, A_n^* is given by

36

$$A_n^* = W_S^* t_S^*$$ (B2)

where W_S^* and t_S^* are the width and thickness of the sample, respectively. Dividing equation (B1) by the length of the SIP-sample, L_S, and solving for $\dot{v}^*/A_n^*$ yields

$$\frac{\dot{v}^*}{A_n^*} = \frac{L_S^*}{s^*} \frac{\Delta p^*}{L_S^*}$$ (B3)

Equation (B3) expresses the volume rate of flow per normal unit area through the SIP in terms of the pressure gradient. This equation can be put into a form analogous to equations (18), which describe the mass flux per unit length through the tile gaps, by multiplying the equation by $\rho^* t_S^*$. Thus,

$$\frac{\rho^* \dot{v}^*}{W_S^*} = \rho^* t_S^* \frac{L_S^*}{s^*} \left(\frac{\Delta p^*}{L_S^*}\right)$$ (B4)

Comparing equation (B3) with equations (18) and (24), we see that

$$\sigma_{SIP}^* = \rho^* t_S^* \frac{L_S^*}{s^*}$$ (B5)

The corresponding tile gap porosity is given by equation (24) as

$$\sigma_{GAP}^* = \frac{\rho^* h^{*3}}{12 \mu^*} = \frac{\rho^* h_r^{*3}}{12 \mu^*} \left(\frac{h^*}{h^*}\right)^3$$ (B6)

The numerical values used for the quantities appearing in equations (B5) and (B6) are

$$S^* = 0.07384 \times 10^4 \; \frac{gm\text{-}cm^2}{sec} \qquad \text{(from ref. 4)}$$

$$L_S^* = 9.525 \; cm \qquad \text{(from ref. 4)}$$

$$t_S^* = 0.41 \; cm \qquad \text{(present TPS geometry)}$$

$$h_r^* = 0.13 \; cm \qquad \text{(present TPS geometry)}$$

$$\rho^* = 1.225 \times 10^{-3} \; gm/cm^3 \qquad \text{(sea-level condition)}$$

$$\mu^* = 1.7894 \times 10^{-4} \; \frac{gm}{cm\text{-}sec} \qquad \text{(sea-level condition)}$$

The values for ρ^* and μ^* correspond to standard sea-level conditions since the SIP porosity measurements documented in reference 4 were acquired under sea-level conditions. Using the above values in equations (B5) and (B6) yields

$$\sigma_{SIP}^* = 6.479 \times 10^{-6} \; cm\text{-}sec$$

$$\sigma_{GAP}^* = 1.253 \times 10^{-3} \left(\frac{h^*}{h_r^*} \right)^3 cm\text{-}sec$$

Figure 3 is a plot of $\log_{10} \left(\sigma_{GAP}^* \Big/ \sigma_{SIP}^* \right)$ versus the gap ratio $h^* \Big/ h_r^*$.

38

APPENDIX C

INCORPORATION OF GAP INTERFACE CONDITION INTO LAPLACE EQUATION SOLVER

The Laplace equation solver used in the current work was an SLOR method written in delta form. In order to implement the interface conditions, equations (19) and (20), only the res₊ial calculation had to be modified. In the notation of figure 5, the residual of the finite-difference analog of equation (8) is

$$S^*_{ij} = (P_{xx})^*_{i,j} + \frac{(p_y)^*_{i,j+1/2} - (p_y)^*_{i,j-1/2}}{\Delta y^*} \tag{C1}$$

The formula for $(p_{xx})^*_{i,j}$ must be slightly modified from its usual central difference form at the $\cdots$ es due to the jump in $(p_x)^*$ there. In the line relaxation procedure, y^* is taken to be the implicit direction and the program solves successive $x^* =$ constant lines from left to right (i.e., around the tile gap) beginning at $x^* = 0$. The solution, p^*, is continuous at all of the tile edges and, at the tile vertical leading edge, this requires a periodic boundary condition,

$$p^*_{1,j} = p^*_{I,j}$$

since we have "unwrapped" the gap.

A relation for $(p_{xx})^*$ valid at a gap interface (i.e., a vertical edge where h^* is discontinuous) is derived as follows. Expand $(p_x)^*$ in a Taylor series on each side of the interface (taken to be at i) as

$$(p_x)^*_{i-1/2,j} = (p_x)^{*^-}_{i,j} - 1/2\Delta x^*(p_{xx})^*_{i,j} + \ldots$$

$$(p_x)^*_{i+1/2,j} = (p_x)^{*^+}_{i,j} + 1/2\Delta x^*(p_{xx})^*_{i,j} + \ldots$$

$$\left.\right\} \qquad (C2)$$

Subtraction of these two series expansions gives (on using eq. (19))

$$(p_{xx})^*_{i,j} = \frac{(p_x)^*_{i+1/2,j} - (p_x)^*_{i-1/2,j} - (p_x)^{*^+}_{i,j}(1-H)}{\Delta x^*} \qquad (C3)$$

while adding equations (C2) using equations (19), and solving for $(p_x)^{*^.}_{i,j}$ gives

$$(p_x)^{*^+}_{i,j} = \frac{(p_x)^*_{i+1/2,j} + (p_x)^*_{i-1/2,j}}{1+H}$$

Substitution of this result into equation (C3), to eliminate $(p_x)^{*^+}_{i,j}$, then yields

$$(p_{xx})^*_{i,j} = \frac{2H(p_x)^*_{i+1/2,j} - 2(p_x)^*_{i-1/2,i}}{(1 + H)\Delta x^*}$$

Finally, use of a central difference formula for the $(p_x)^*$ which remain gives the following equation for $(p_{xx})^\bullet$, in terms of p^*, as

$$(p_{xx})^*_{i,j} = \frac{H p^*_{i+1,j} - (1+H) p^*_{i,j} + p^*_{i-1,j}}{1/2(1+H)\Delta x^{*2}} \qquad (C4)$$

Equation (C4) is used in equation (C1) to give the required relation for S^*_{ij}. Note that, on grid lines where $H = 1$, equation (C4) reduces to the usual central-difference formula for $(p_{xx})^*$. Along grid lines, where the gap width changes discontinuously, the appropriate value of H is used.

Table I.- Summary of te OS-52 runs selected for comparison witn theory.

Run No.	Tile Thickness	M_∞
28:6	2.5 in	0.840
31:4	"	0.842
34:5	"	0.858
42:3	3.5 in	0.841
43:3	"	0.858
42:9	"	0.867

Flow

A

A
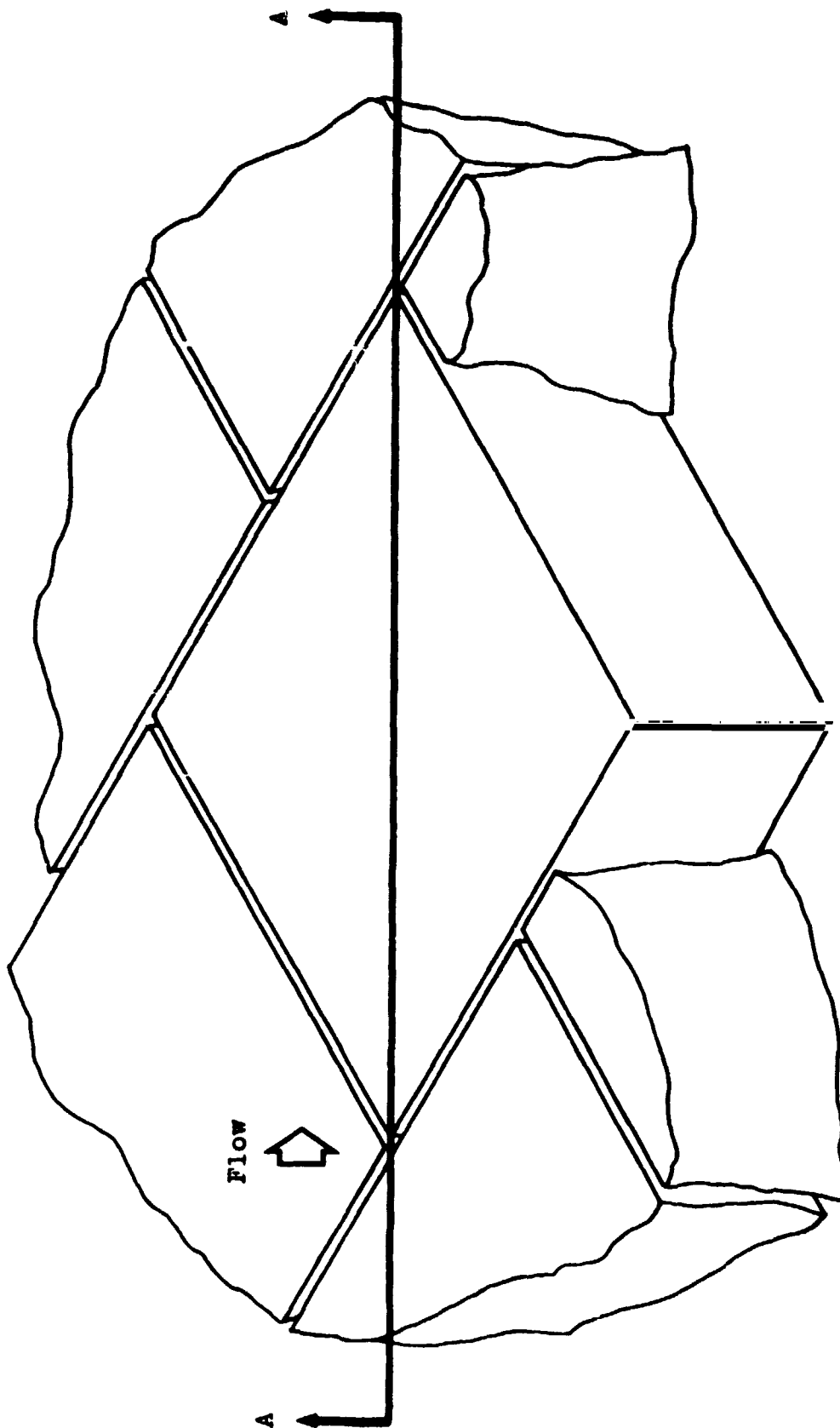
(a) Cutaway view.

Figure 1.- Typical TPS component arrangement.

43
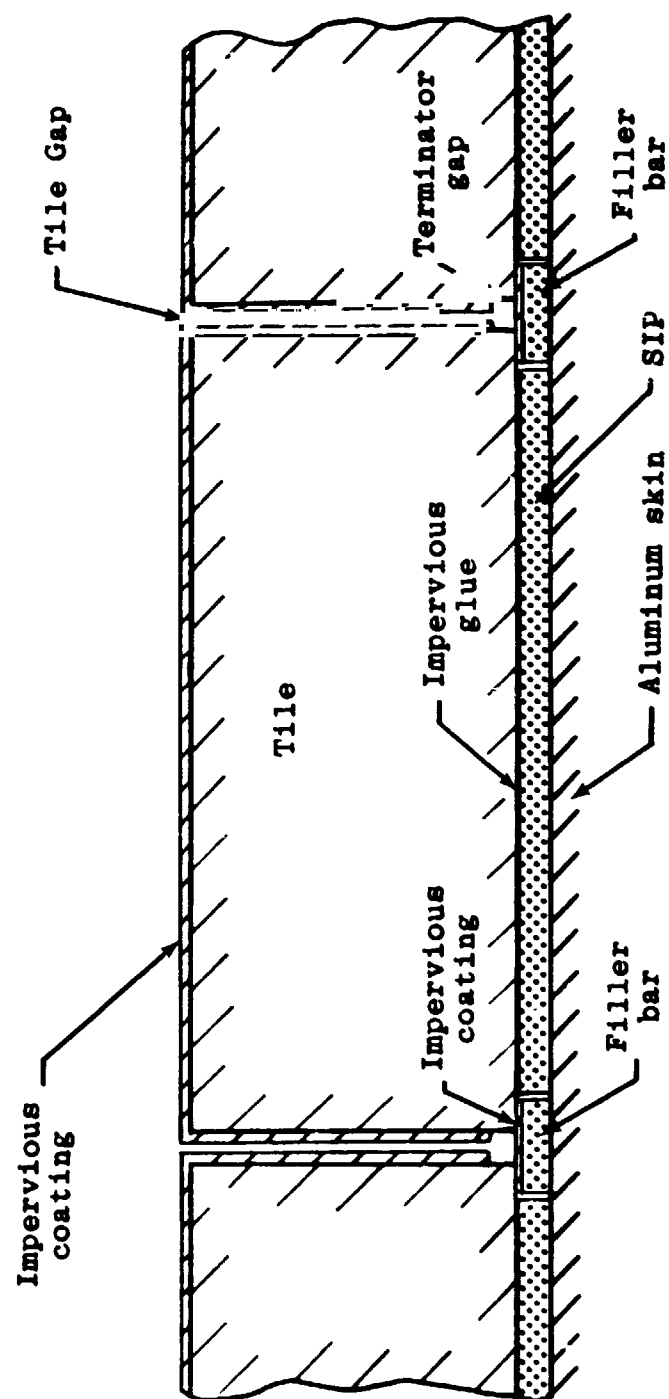
(b) Section A-A.

Figure 1. - Concluded.

x^* - around tile gap
y^* - tile base to tile outer surface
z^* - normal to tile-gap face
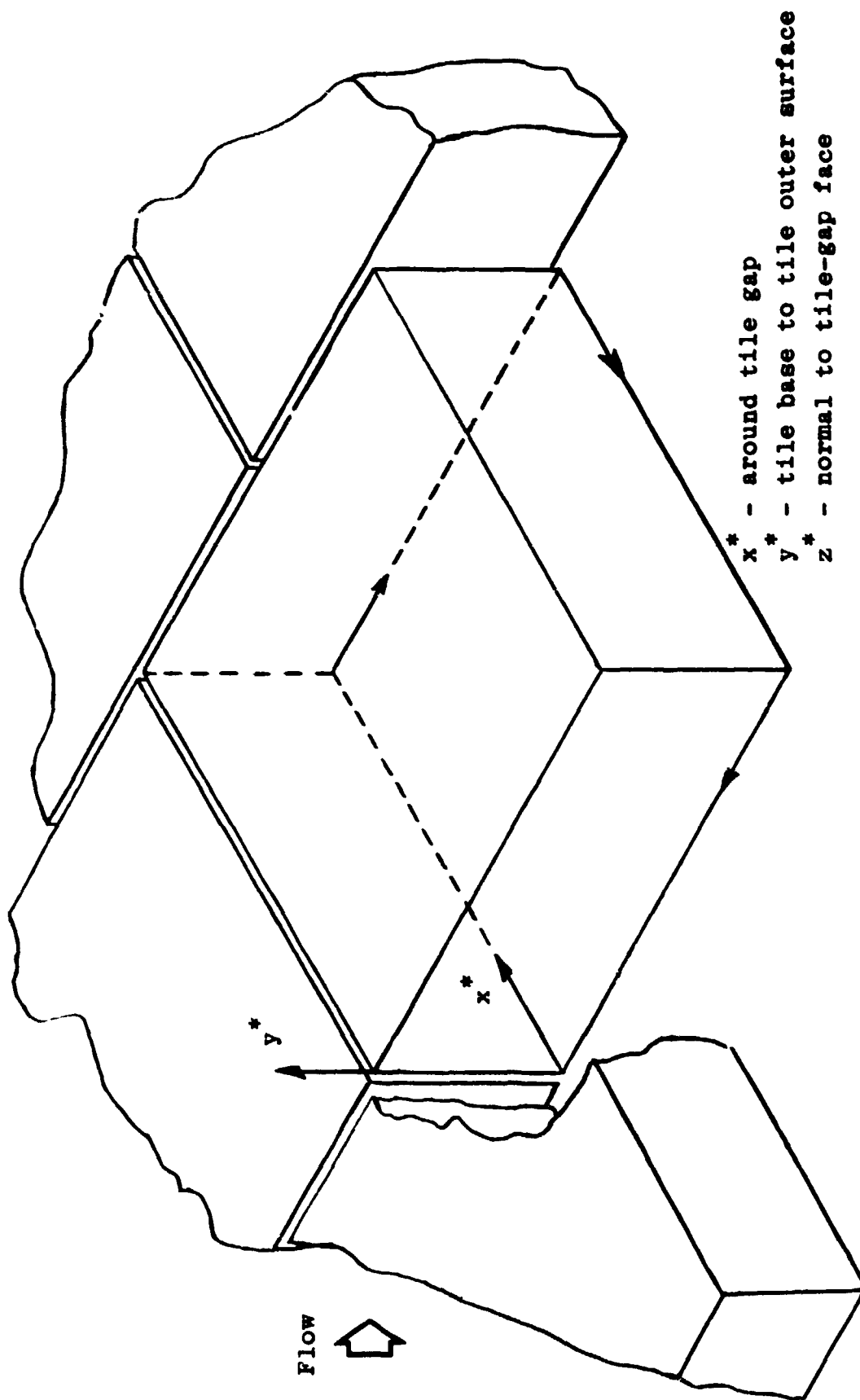
Figure 2.- Tile coordinate system.

45
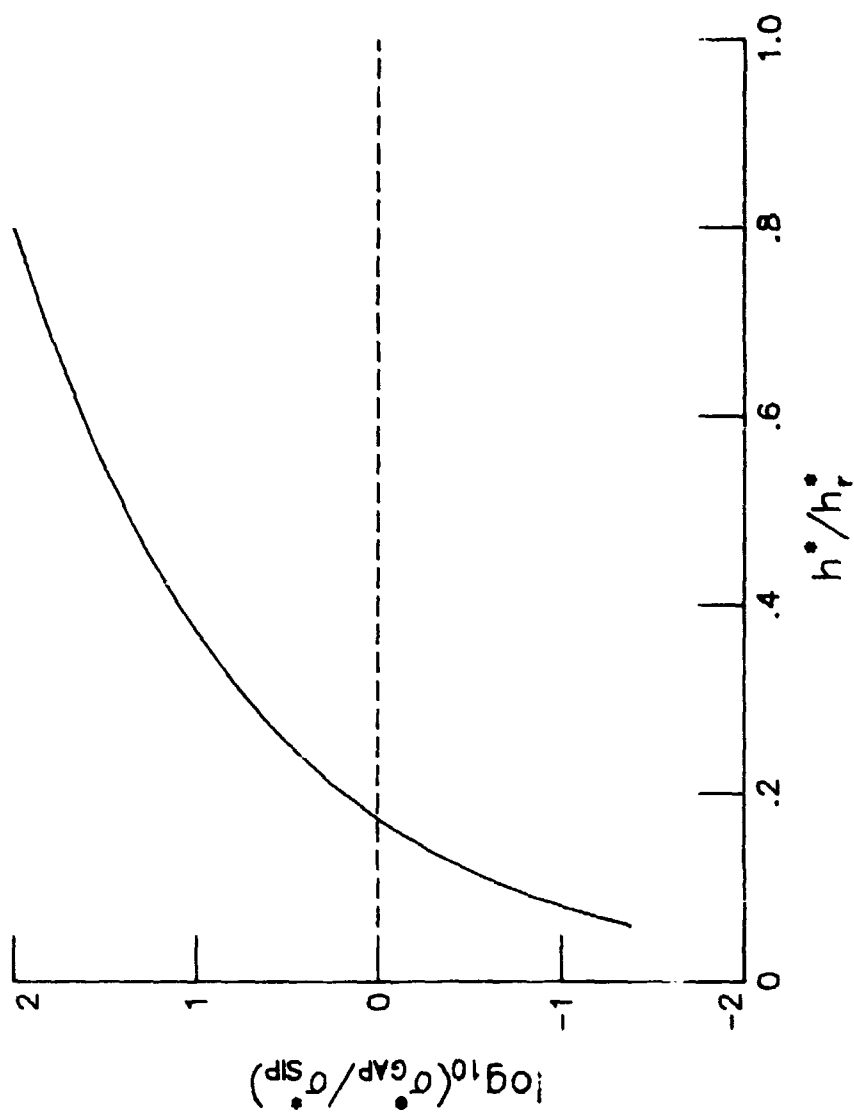
Figure 3.- Computed sea-level tile-gap porosity normalized by SIP porosity (σ_{SIP} = 6.479 × 10^{-6} cm-sec; see Appendix B).
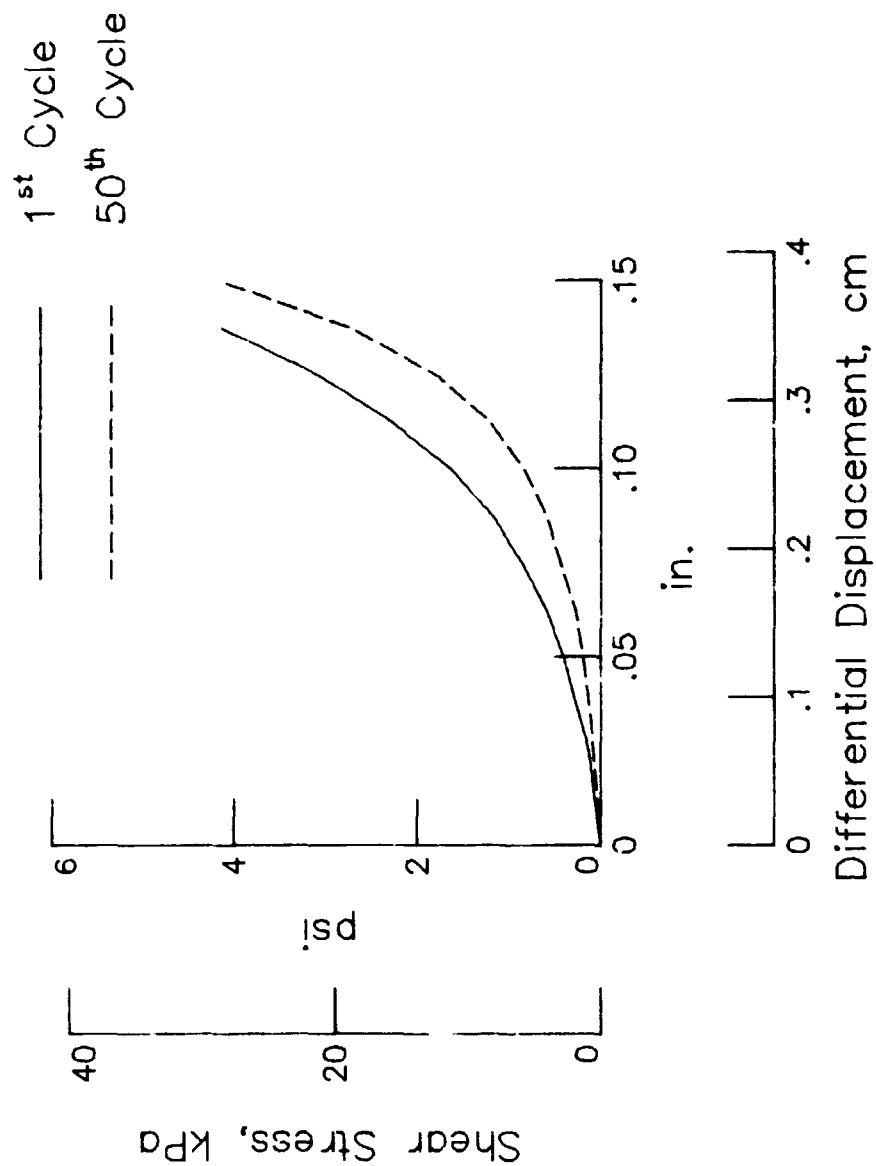
Figure 4.— Shear stress—differential displacement behavior for virgin and load conditioned 0.41-cm (0.16-in) thick SIP. Material stressed in cross-roll direction, cyclic load level = 34.5 kPa (5 psi); from reference 5.

47
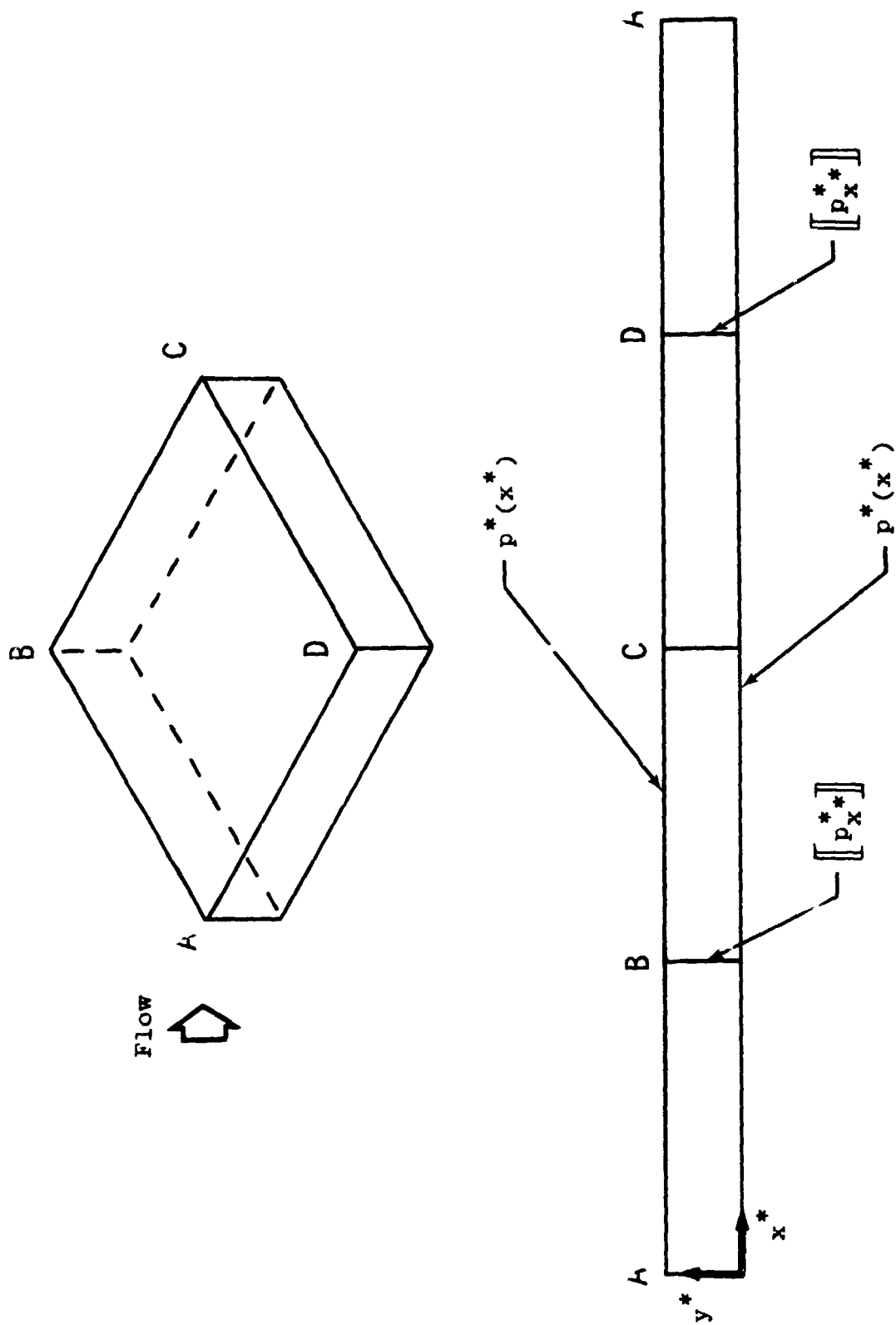
Figure 5. - Tile-gap computation domain for Laplace equation solution.
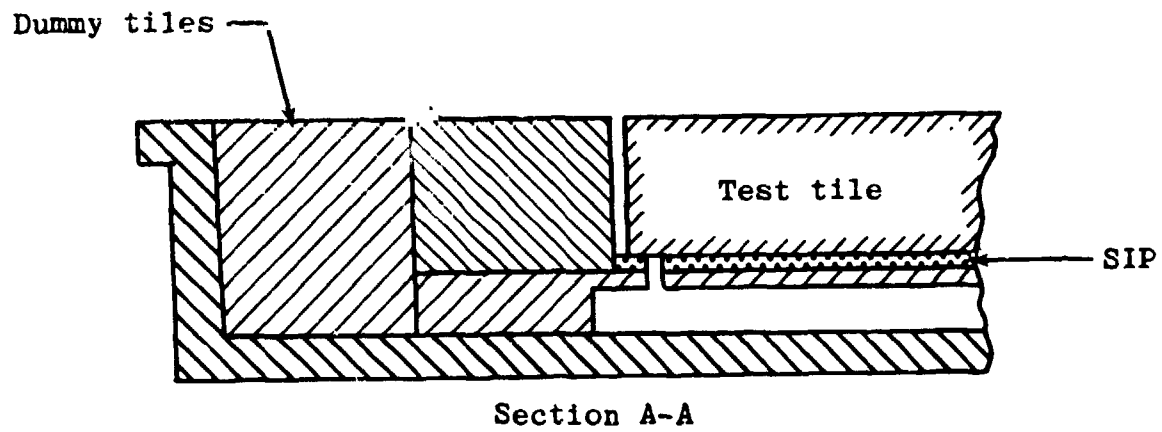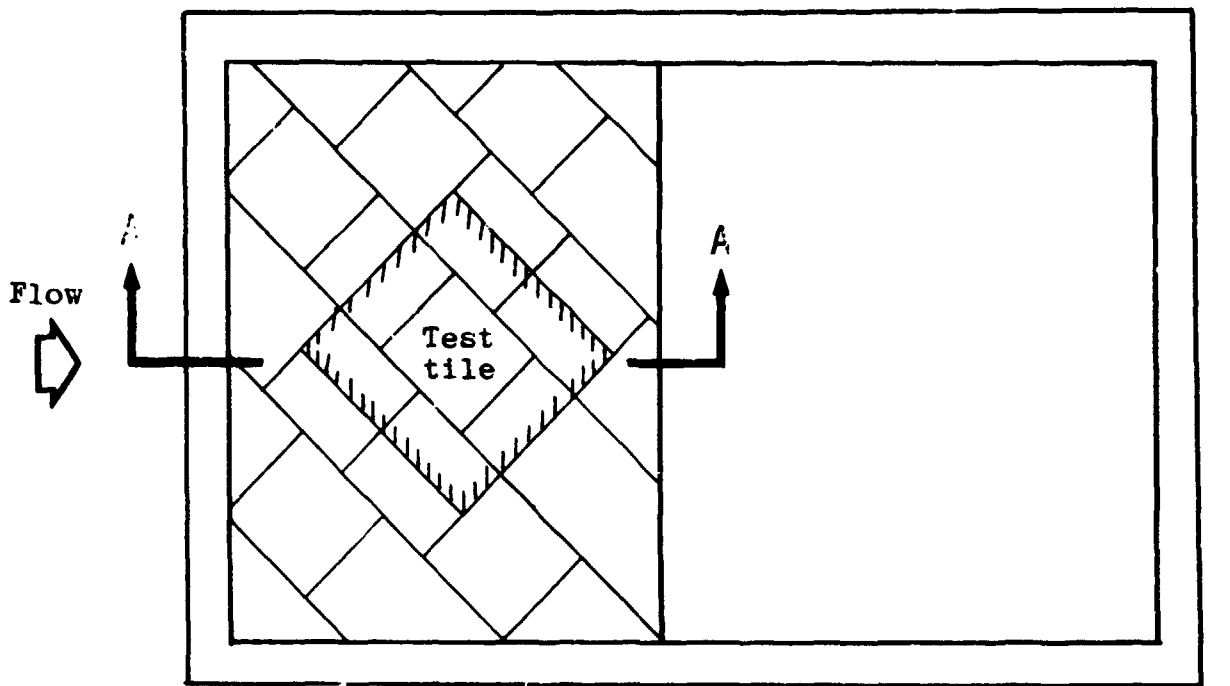
Figure 6.- OS-52 test panel for net airloads experiment.
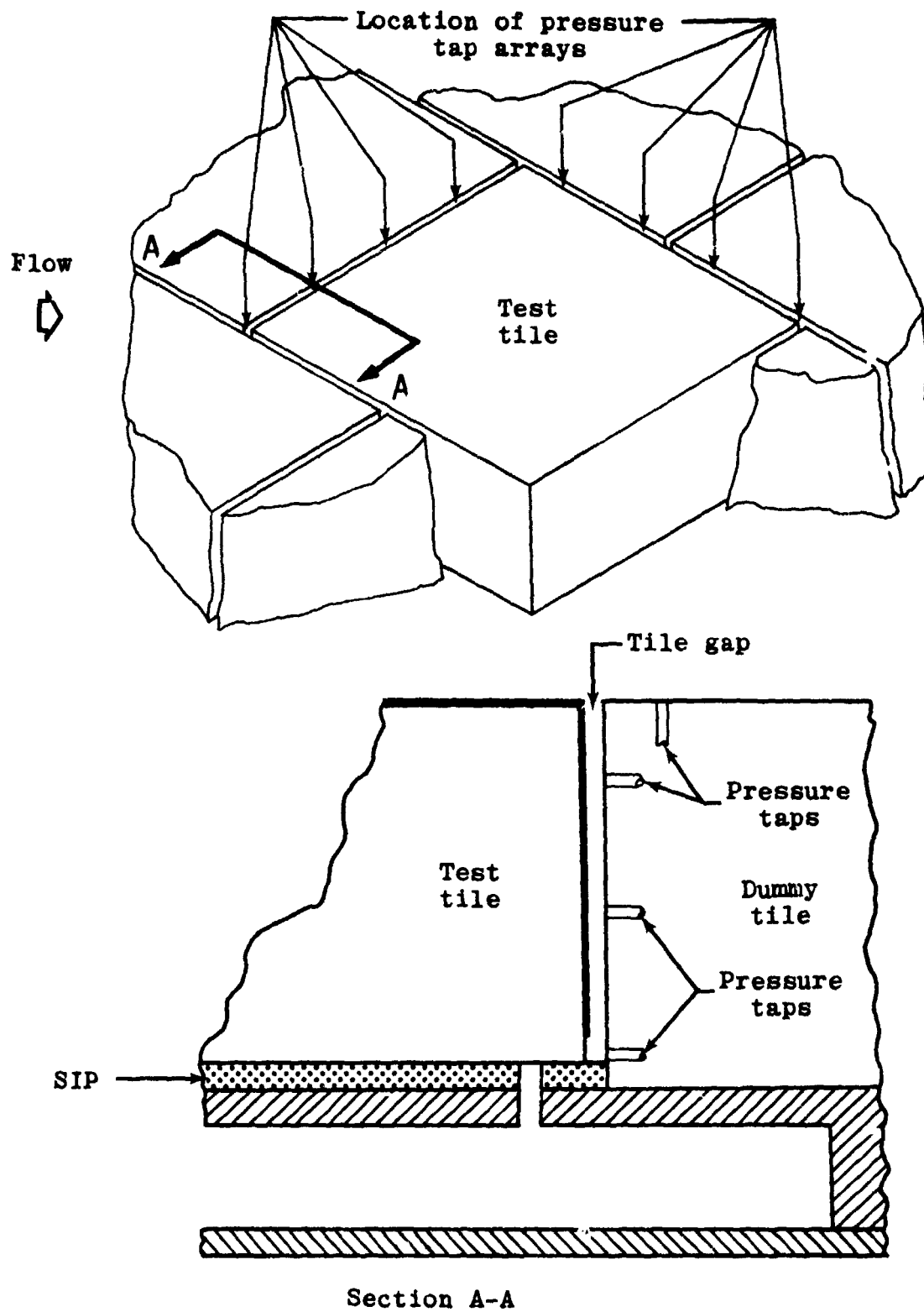
Figure 7.- Locations of tile-gap pressure taps on OS-52 test panel.
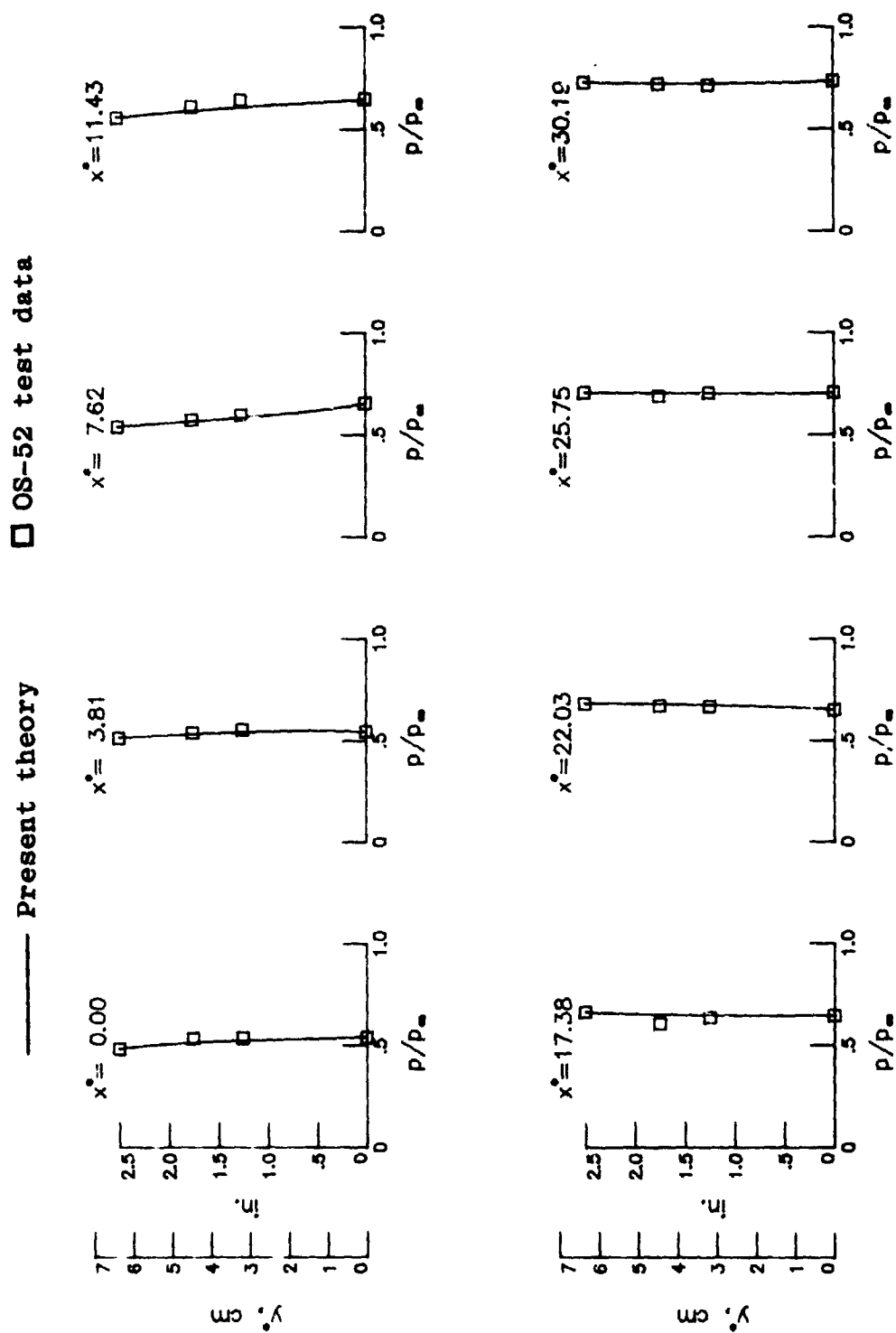
Figure 8.- Comparison of OS-52 test data and calculated tile-gap vertical pressure distributions.

(a) Run 28:6.

51
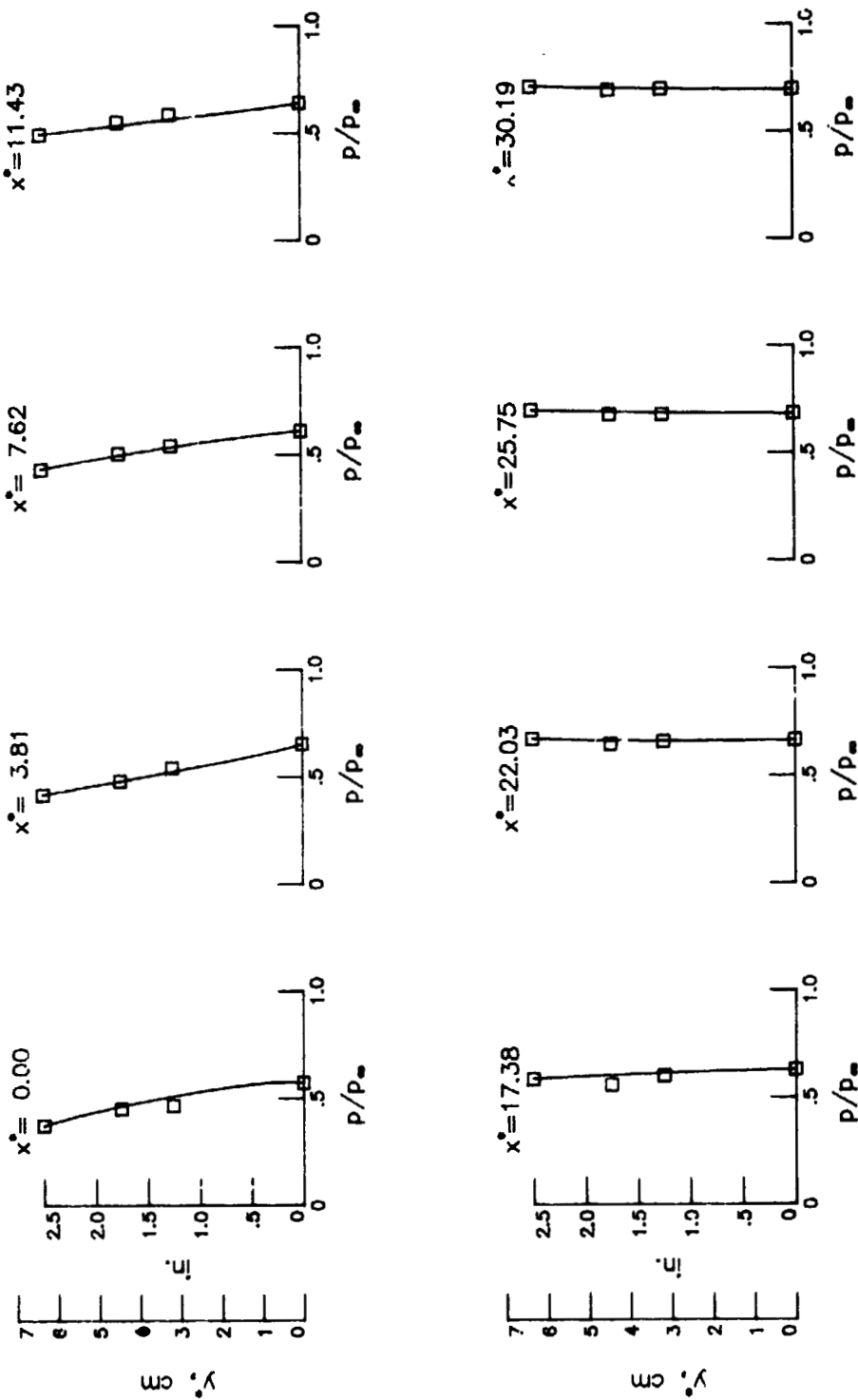
(b) Run 31:4.

Figure 8.- Continued.

52

— Present theory   □ OS-52 test data
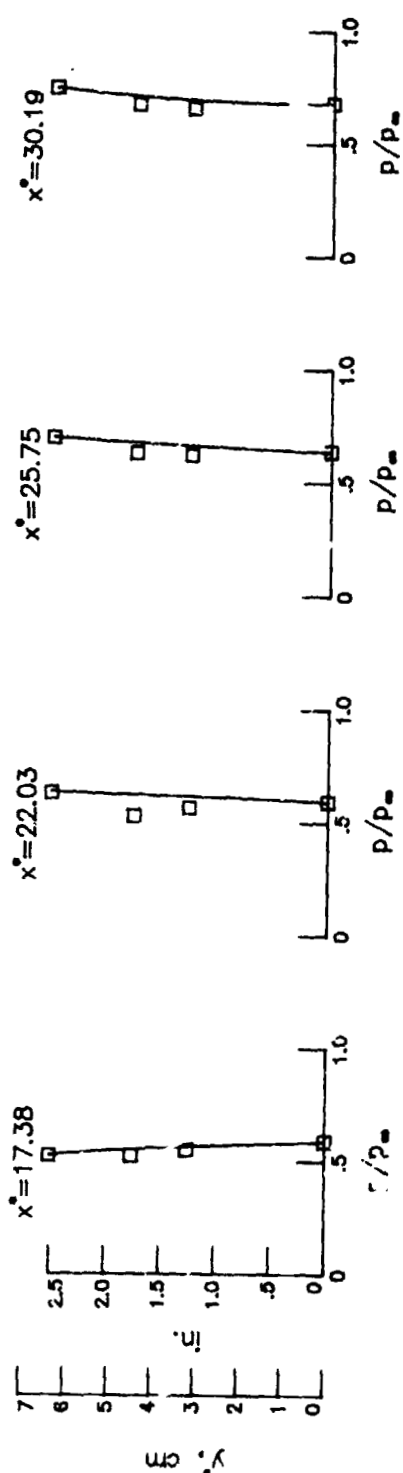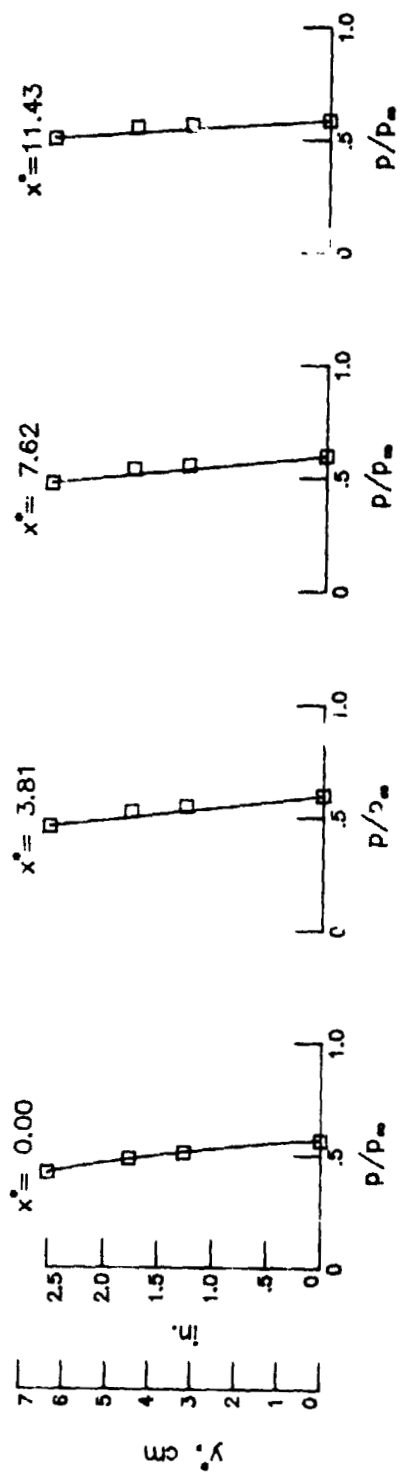
(c) Run 34:5

Figure 8.- Continued.

53
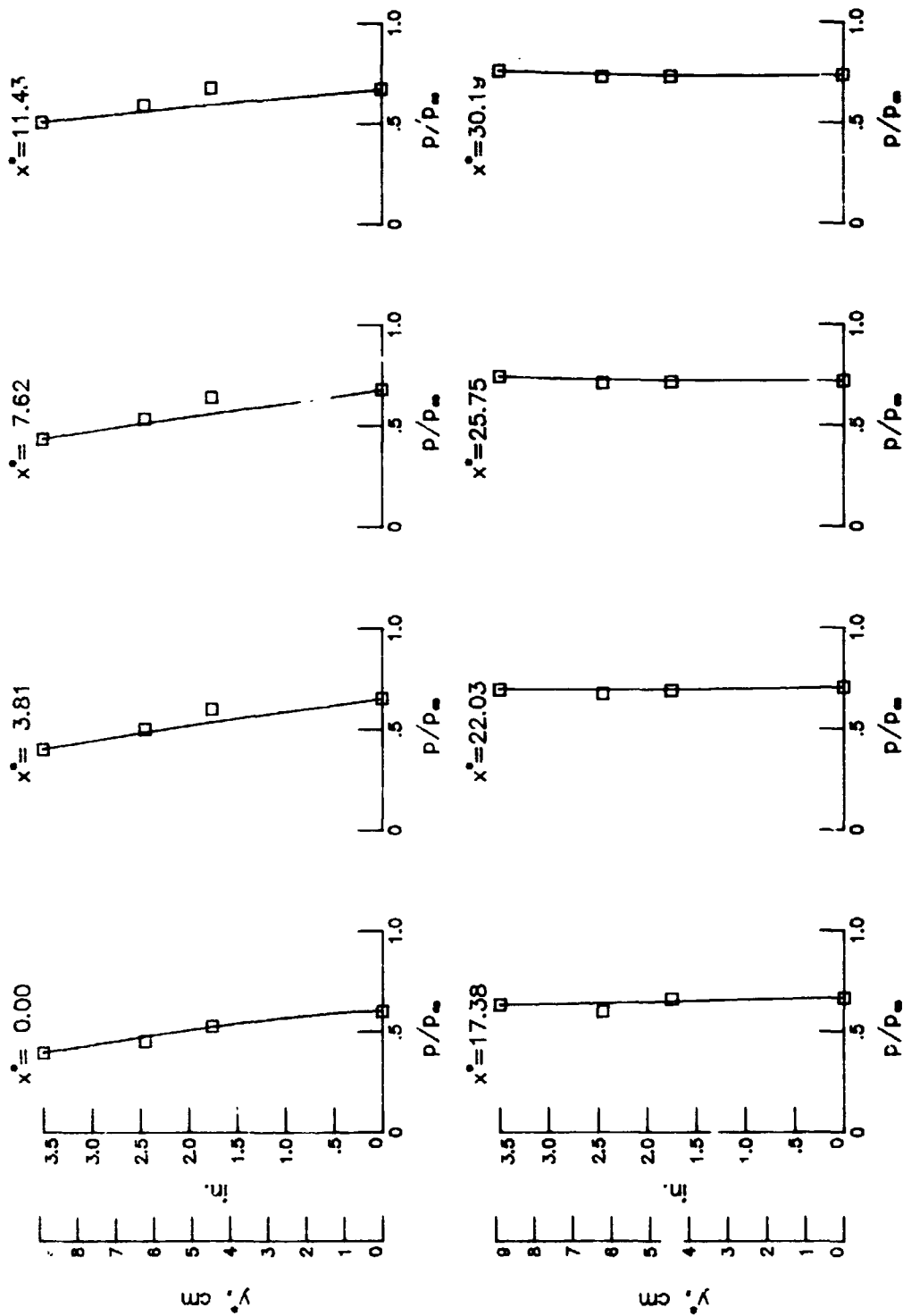
(d) Run 42:3.

Figure 8.- Continued.

54

□ OS-52 test data
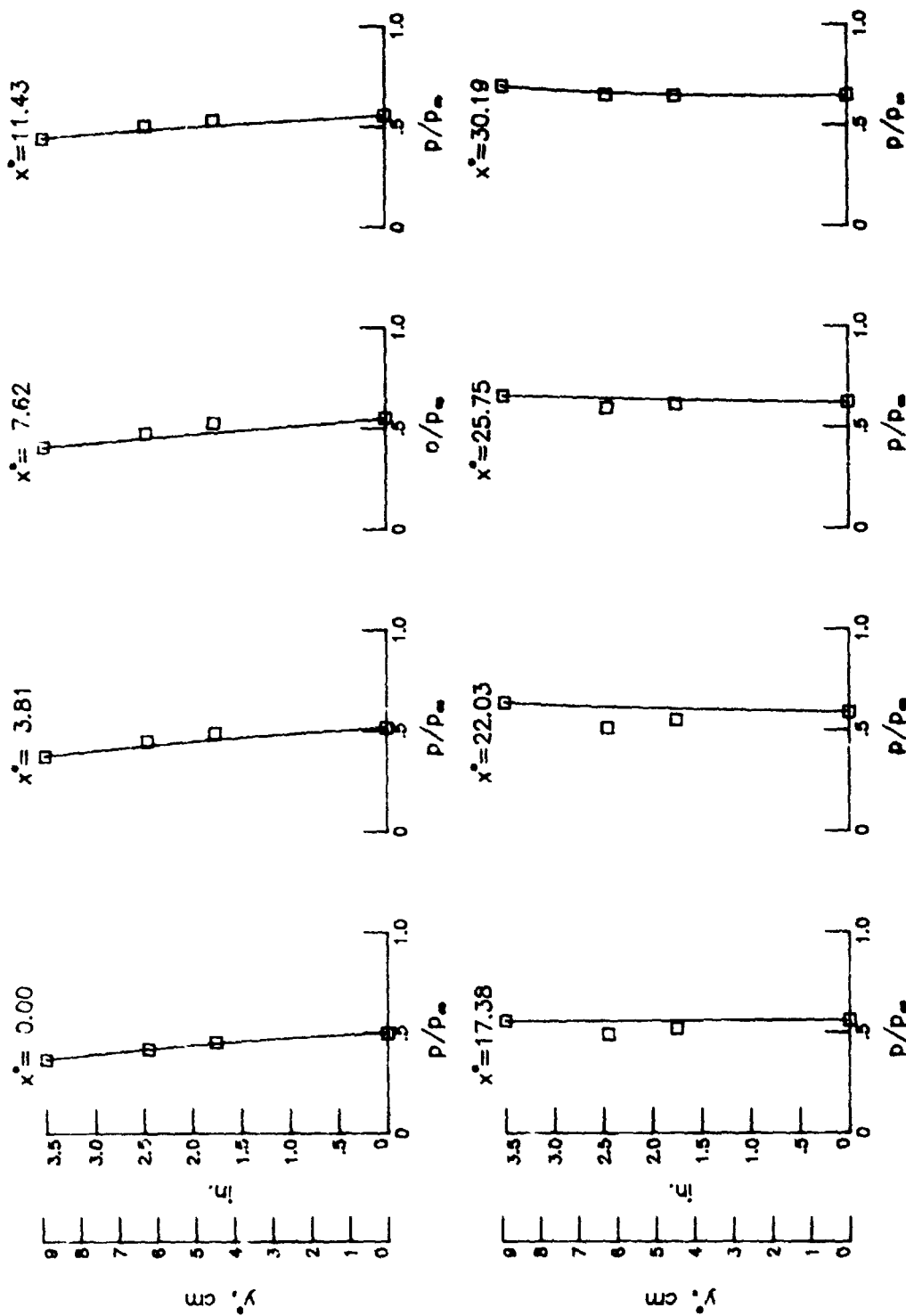
—— Present theory

(e) Run 43:3.

Figure 8.- Continued.

55

□ OS-52 test data

—— Present theory

$x^* = 0.00$ $x^* = 3.81$ $x^* = 7.62$ $x^* = 11.43$

$x^* = 17.38$ $x^* = 22.03$ $x^* = 25.75$ $x^* = 30.19$

p/p_∞

y, cm

(f) Run 42:9.

Figure 8.- Concluded.

(a) H = 1.0.

Figure 9.- Effect of varying H on calculated pressure ratio (p/p$_\infty$) contours.
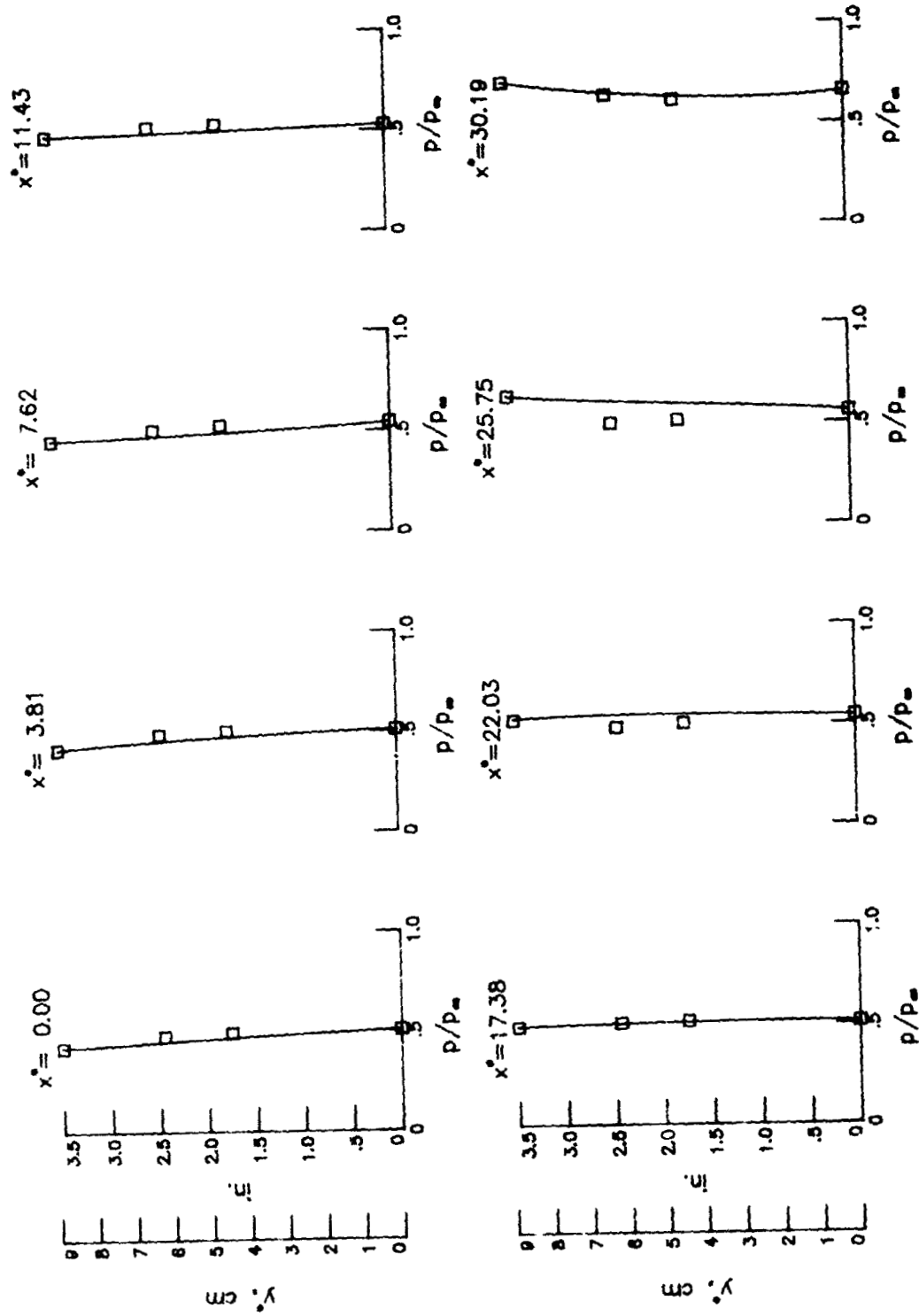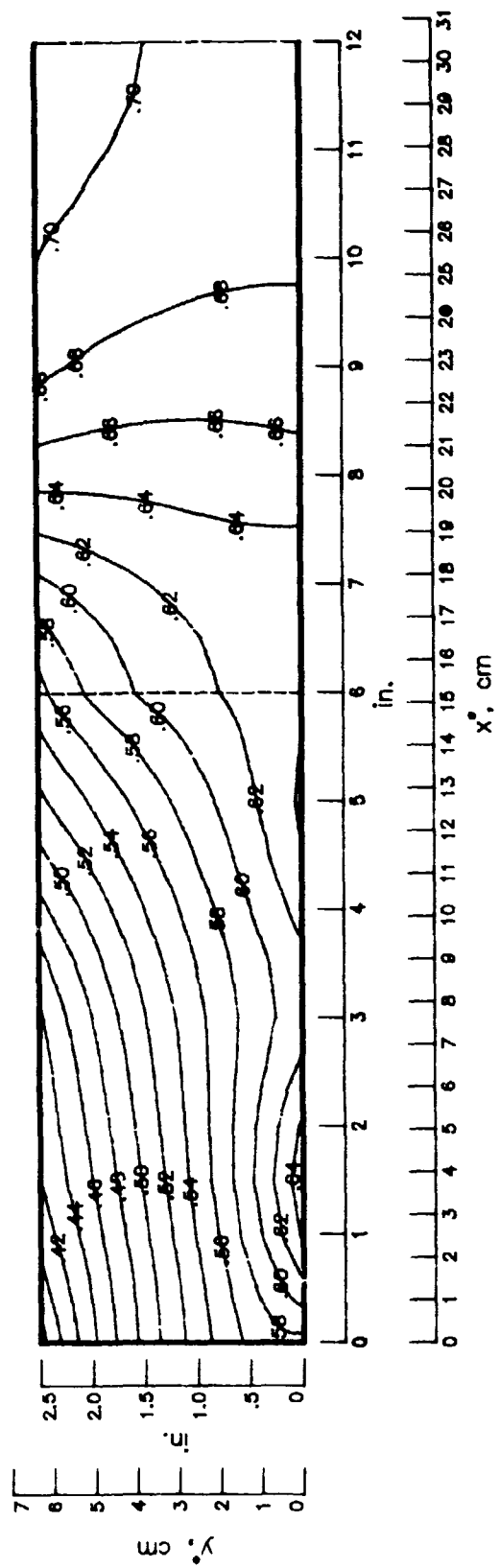
(b) H = 8.0.
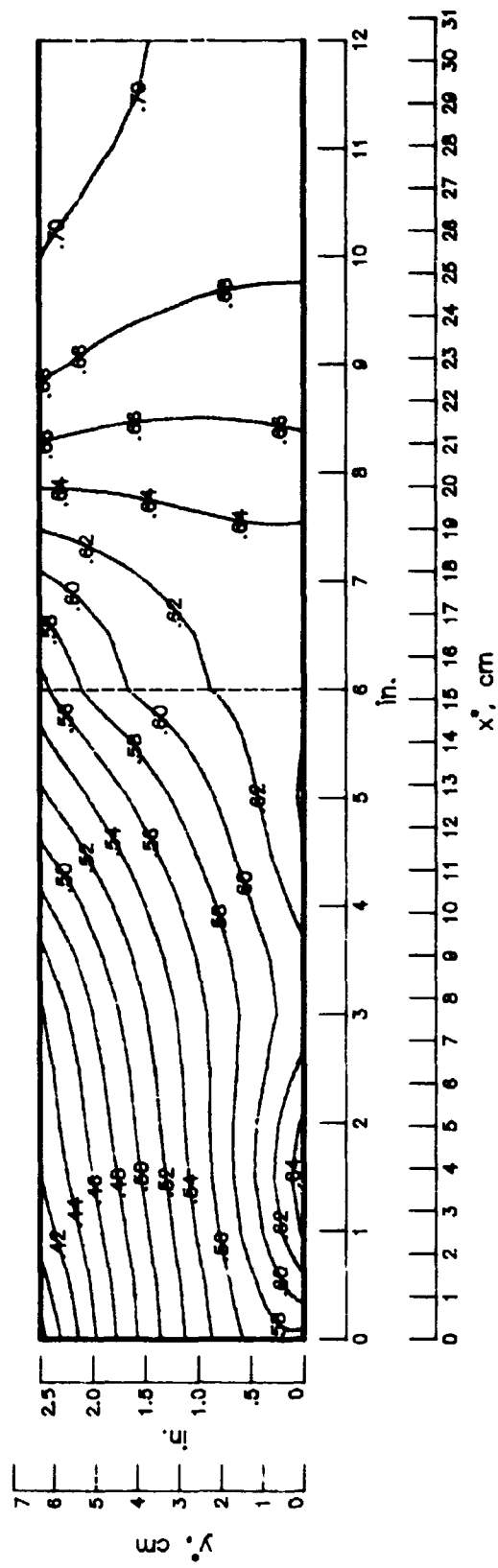
Figure 9.- Continued.

(c) H = 27.0.

Figure 9.- Continued.
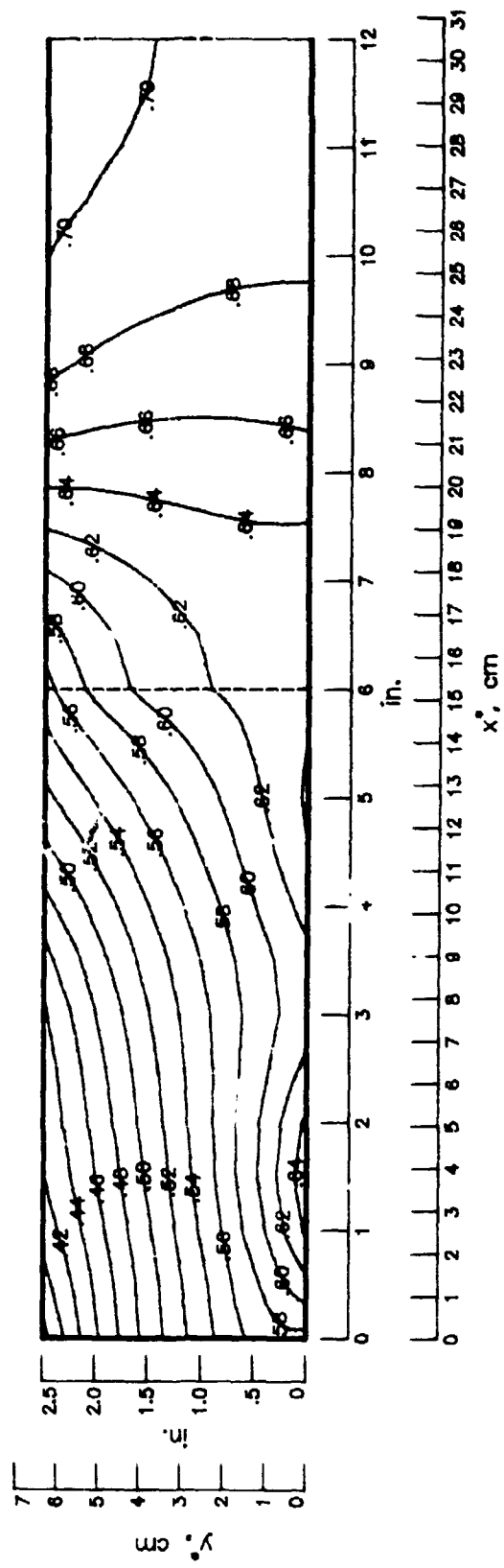
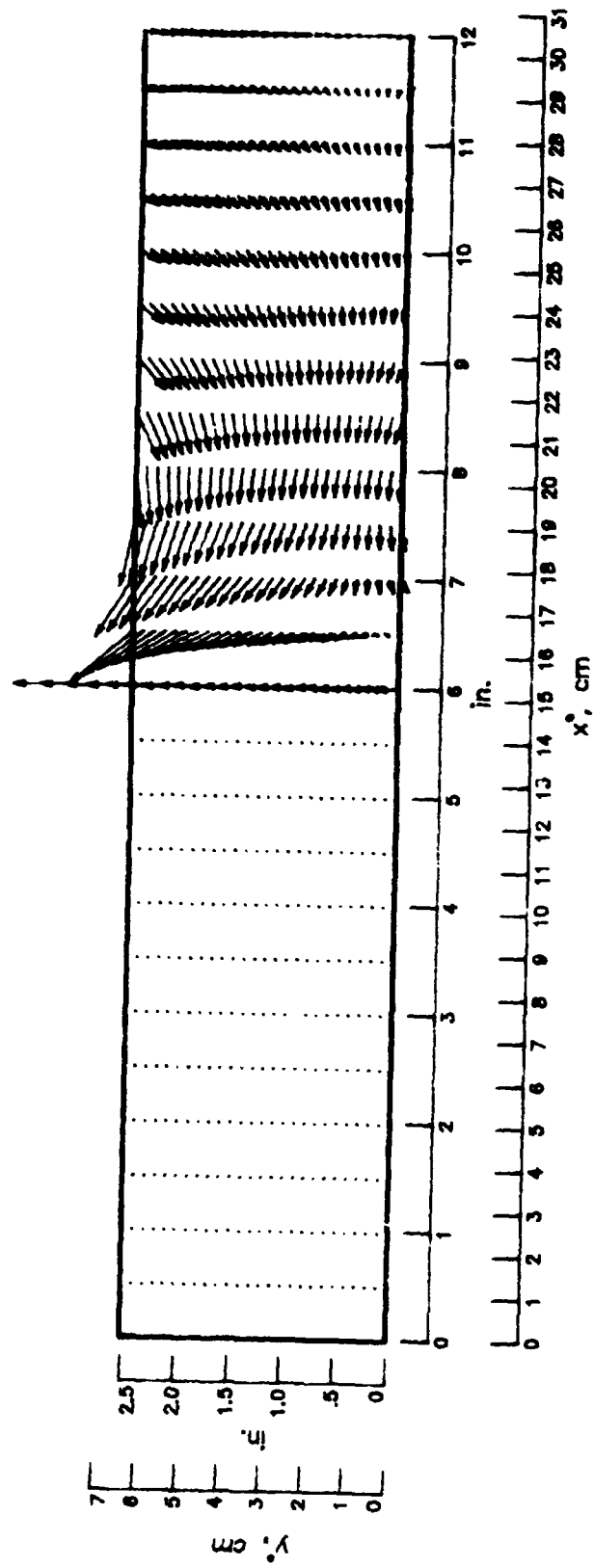(d) H = 64.0.

Figure 9.- Continued.

60
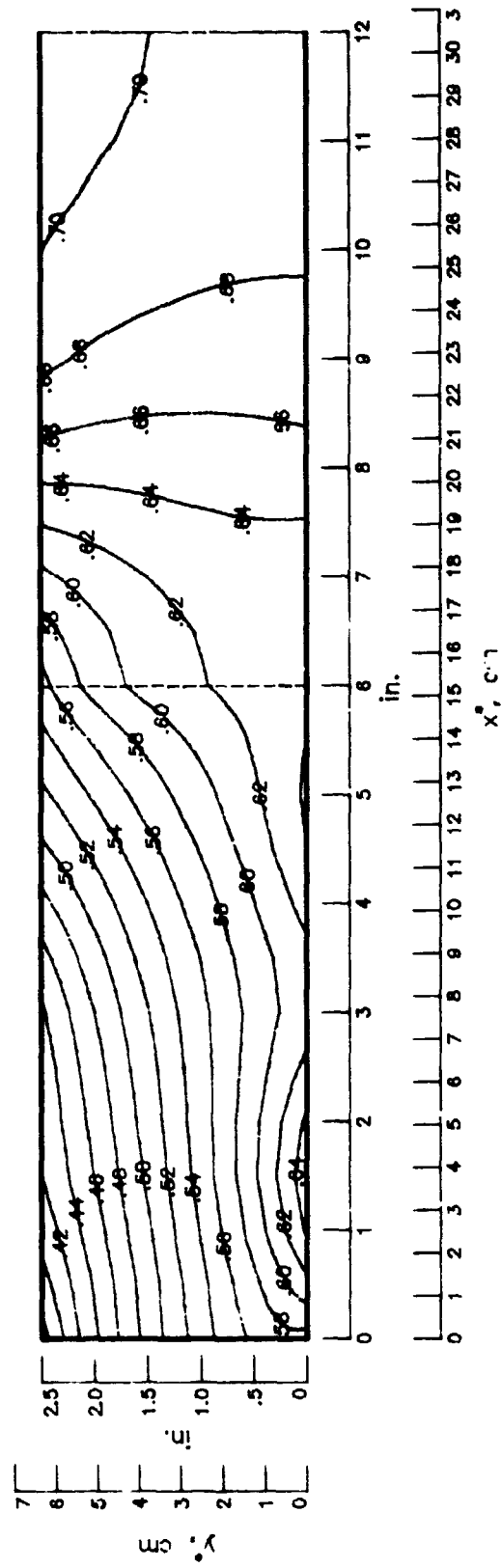
(e) H = 125.0.
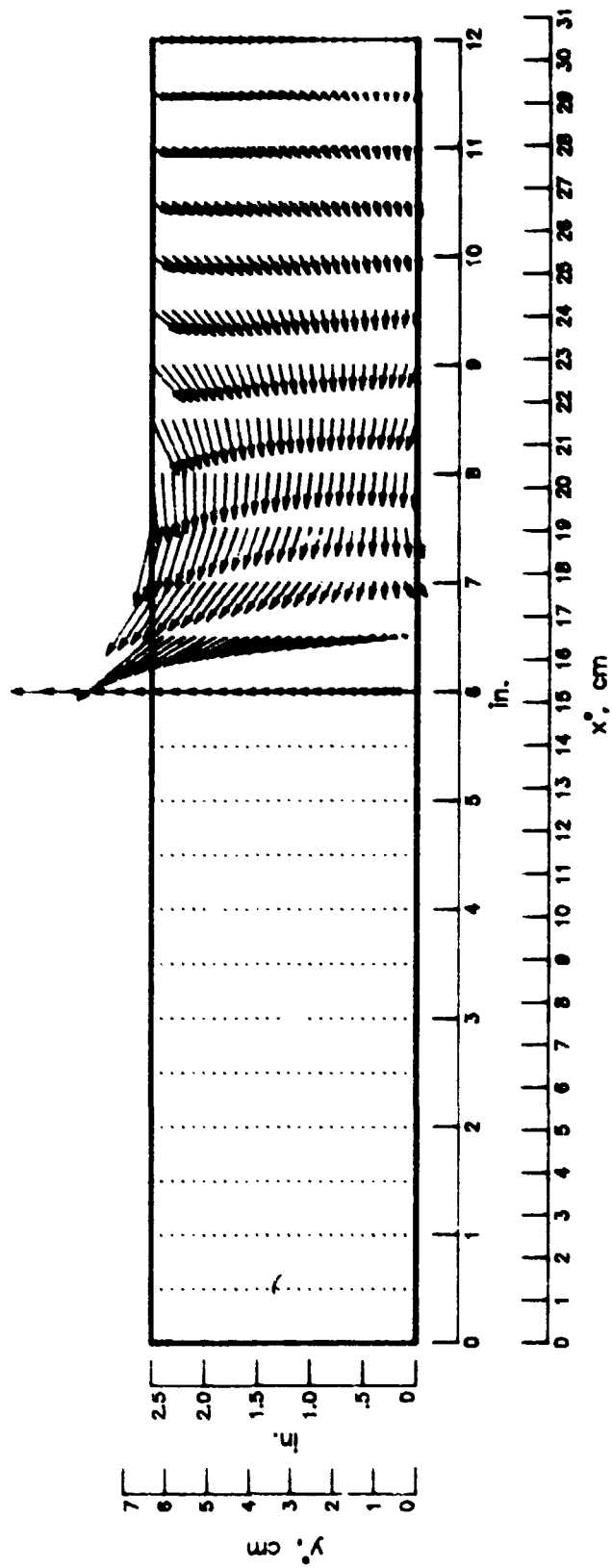
Figure 9.- Continued.
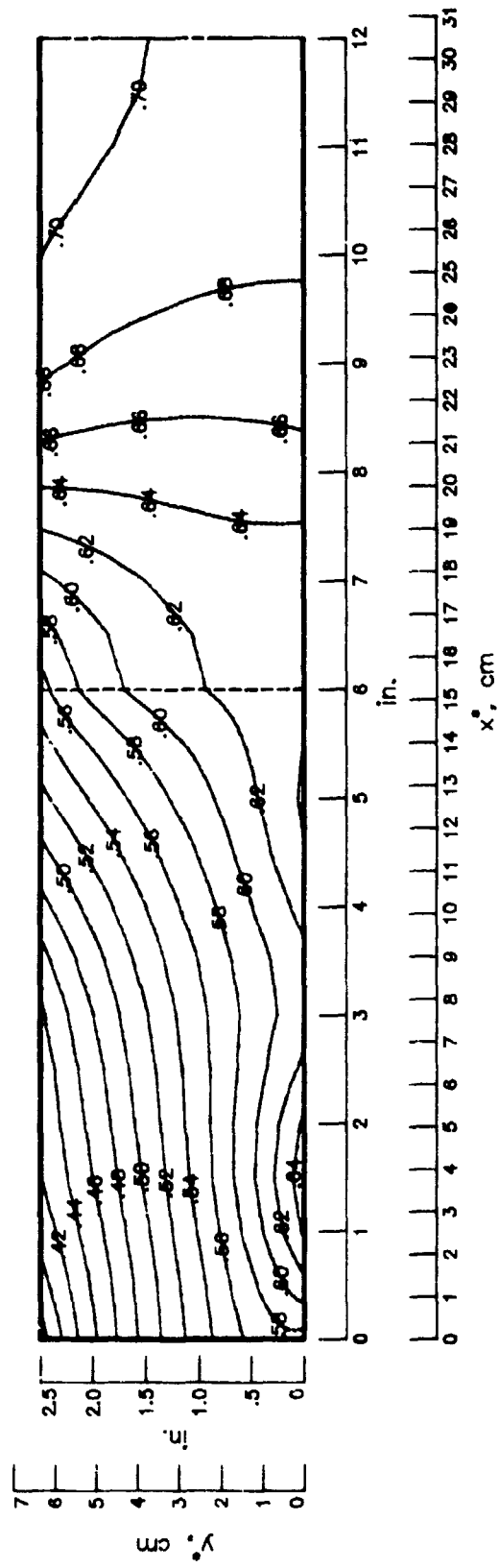
(f) H = 216.0.

Figure 9. - Continued.

62
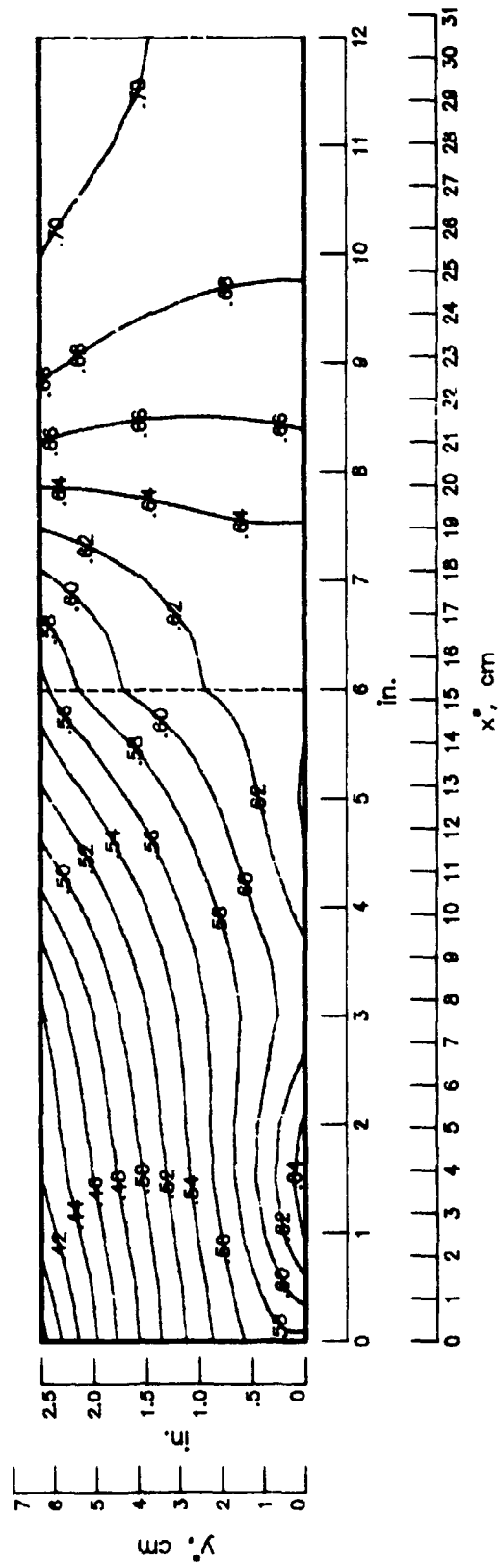
(g) $H = 512.0$.

Figure 9.- Continued.

63
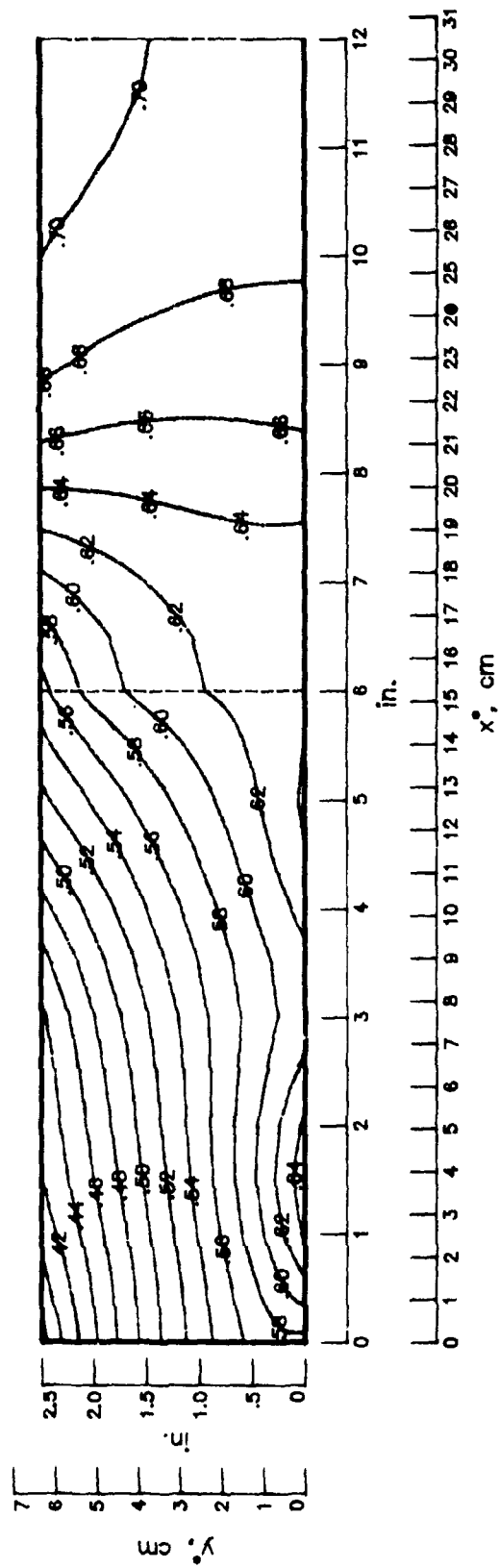
(h) H = 4096.0.

Figure 9.- Concluded.
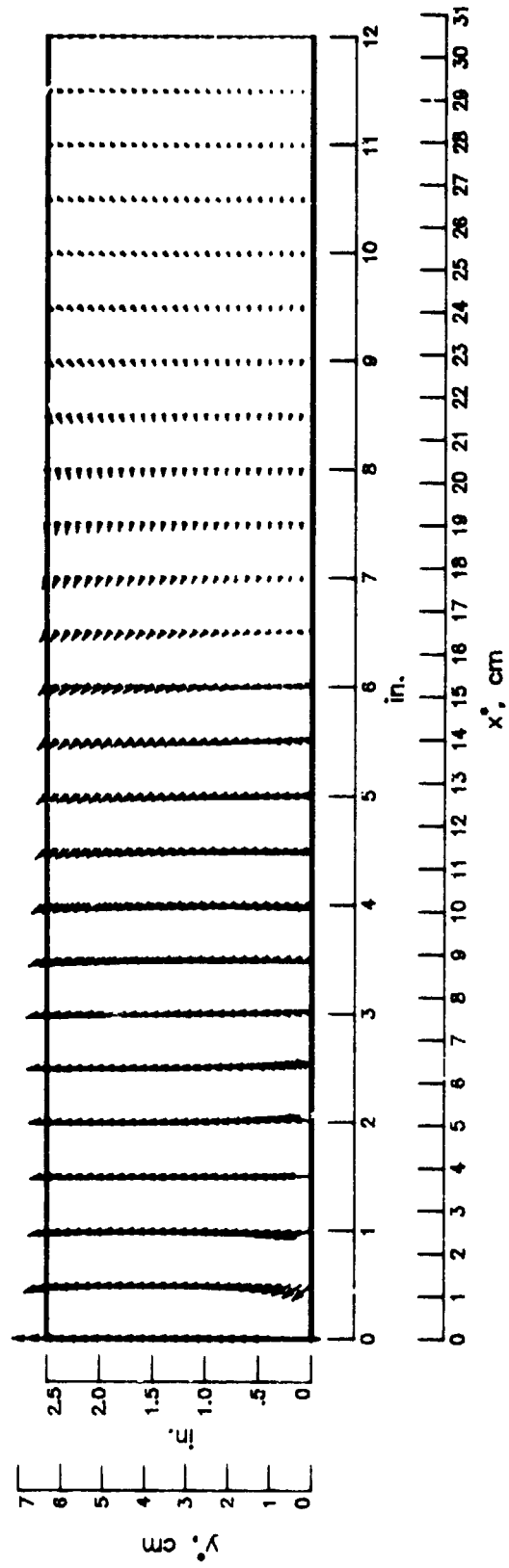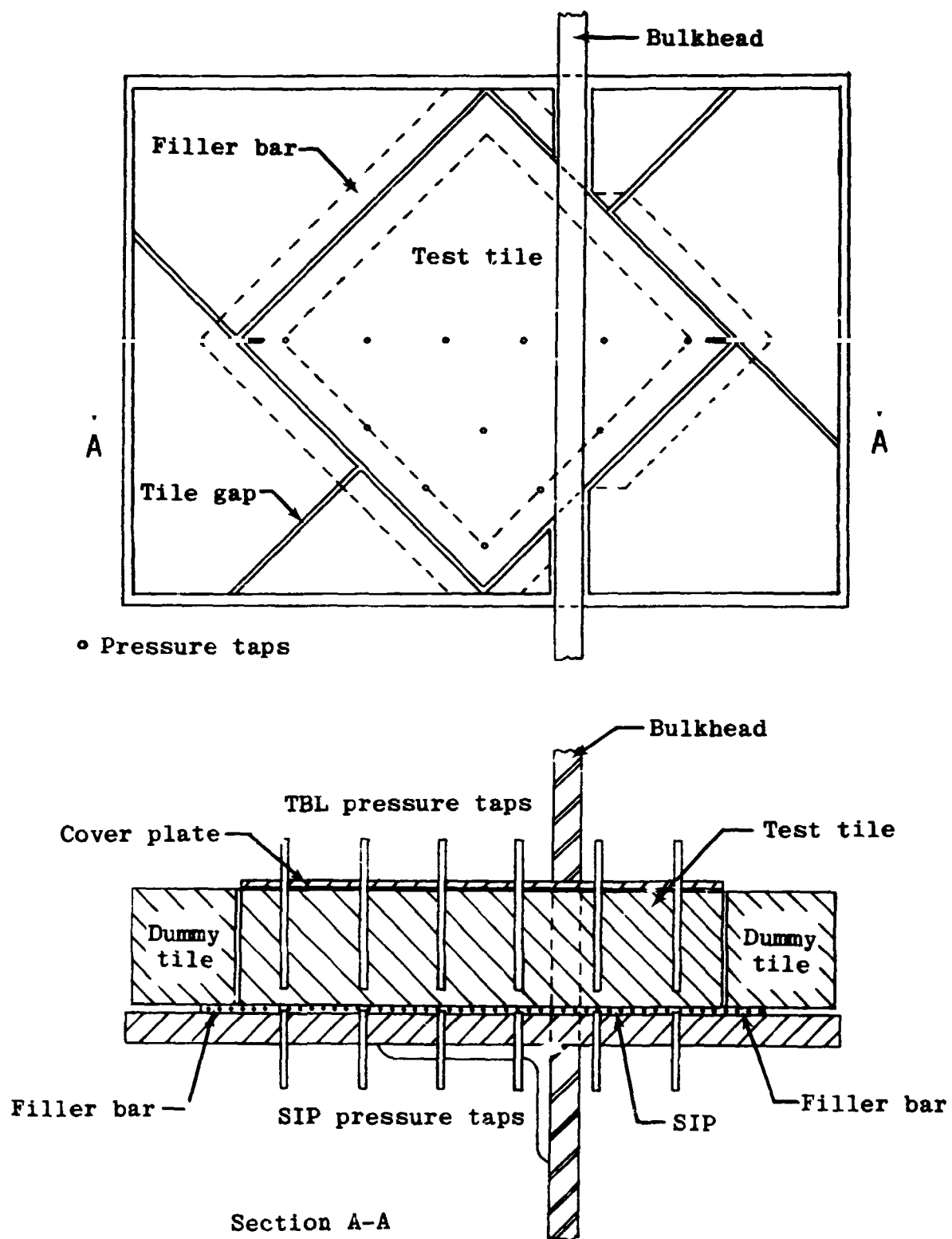
(a) H = 1.0.

Figure 10.- Effect of varying H on calculated normalized mass-flux vectors.
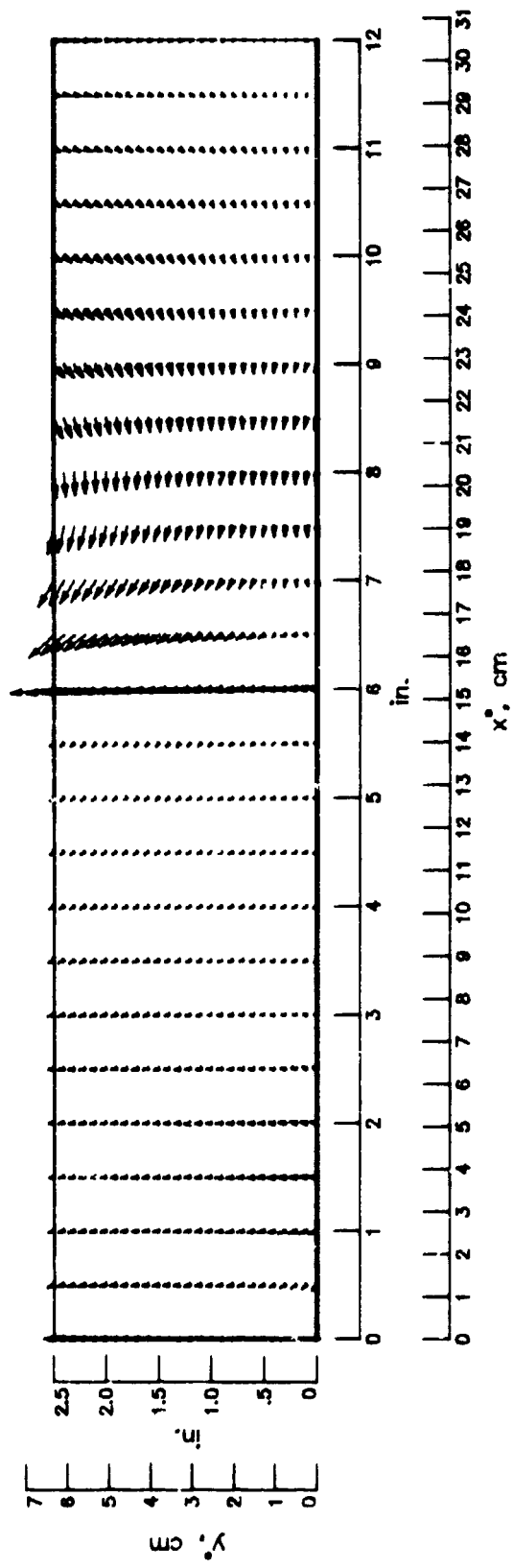
(b) H = 3.0.

Figure 10 - Continued
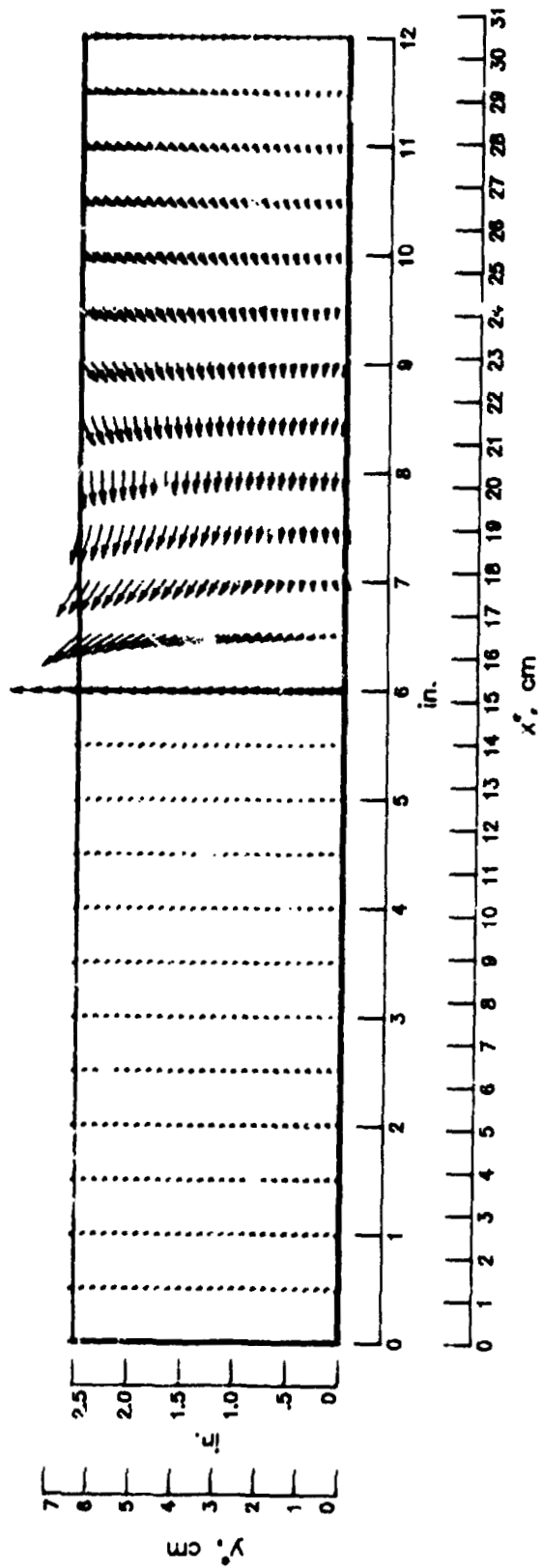
(c) H = 27.0

Figure 10.- Continued.
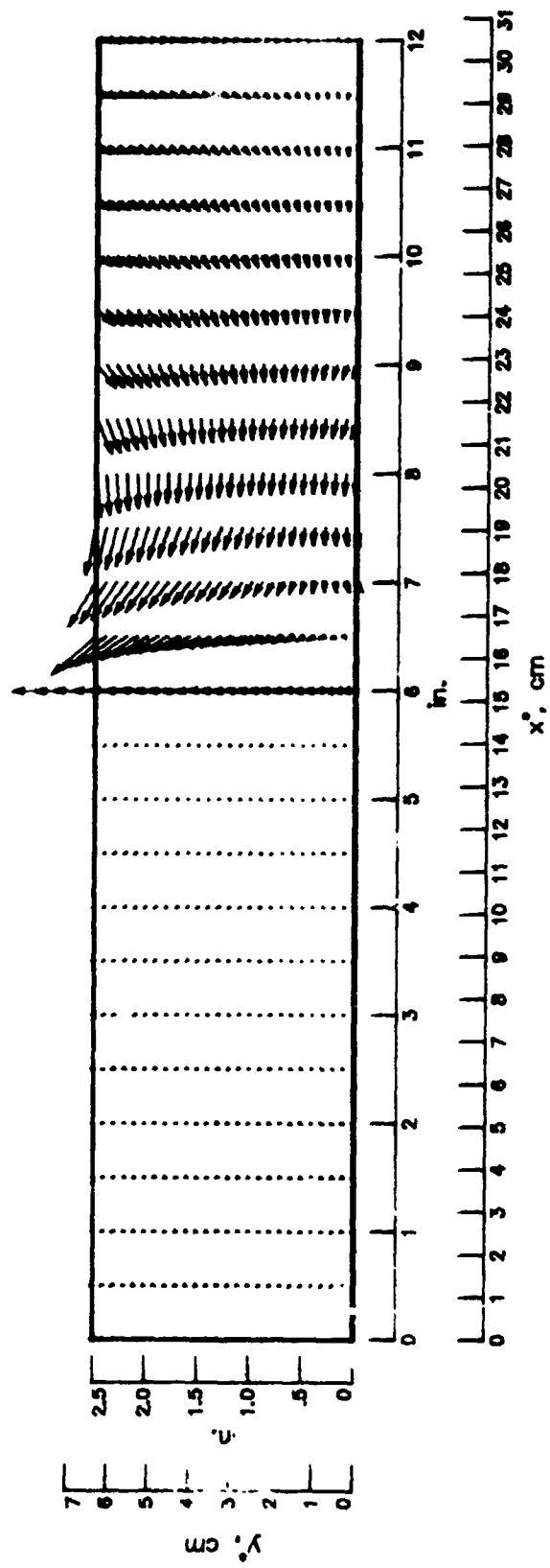
(d) H = 64.0.

Figure 10.- Continued.
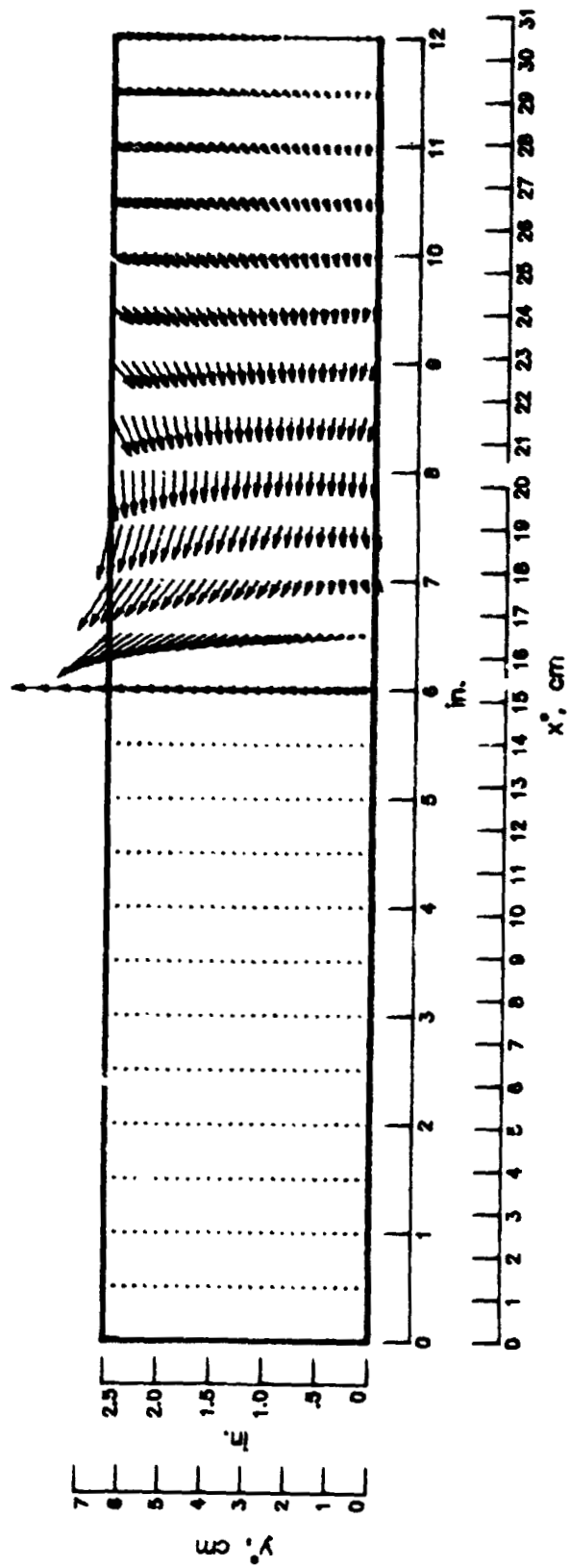
(e) H = 125.0.

Figure 10.- Continued.
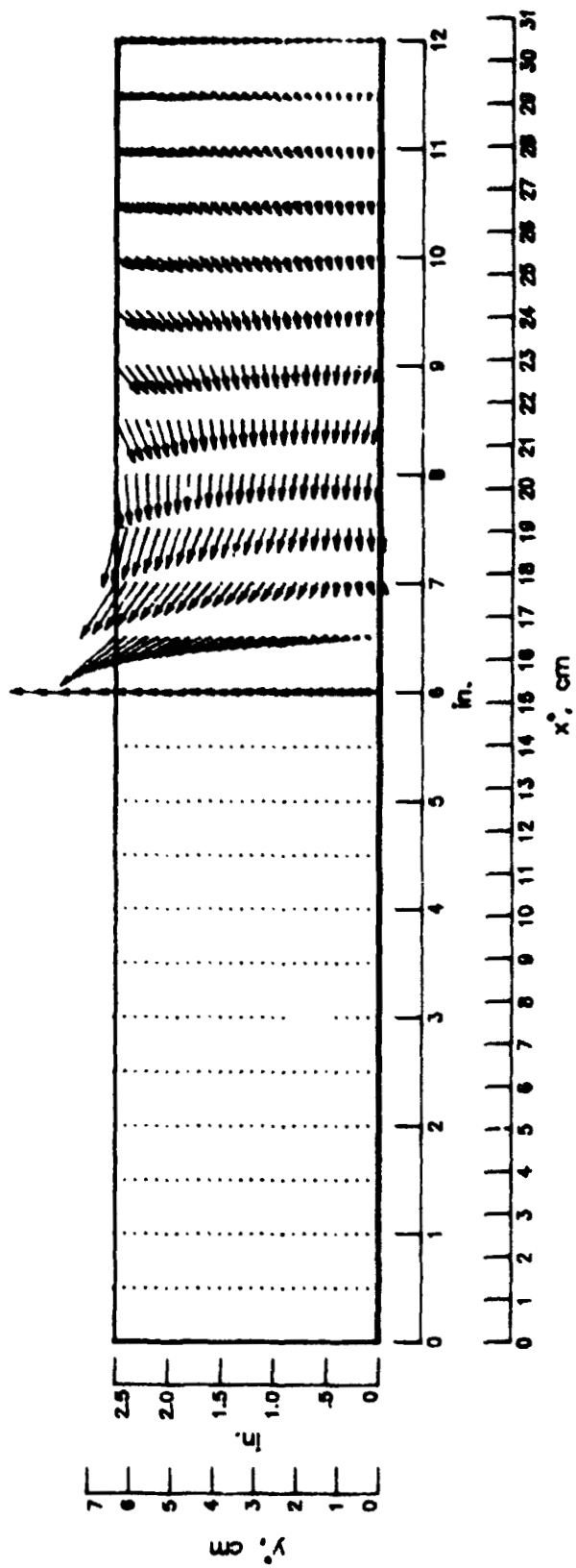
(f) H = 216.0.

Figure 10.- Continued.

(g) H = 512.0.

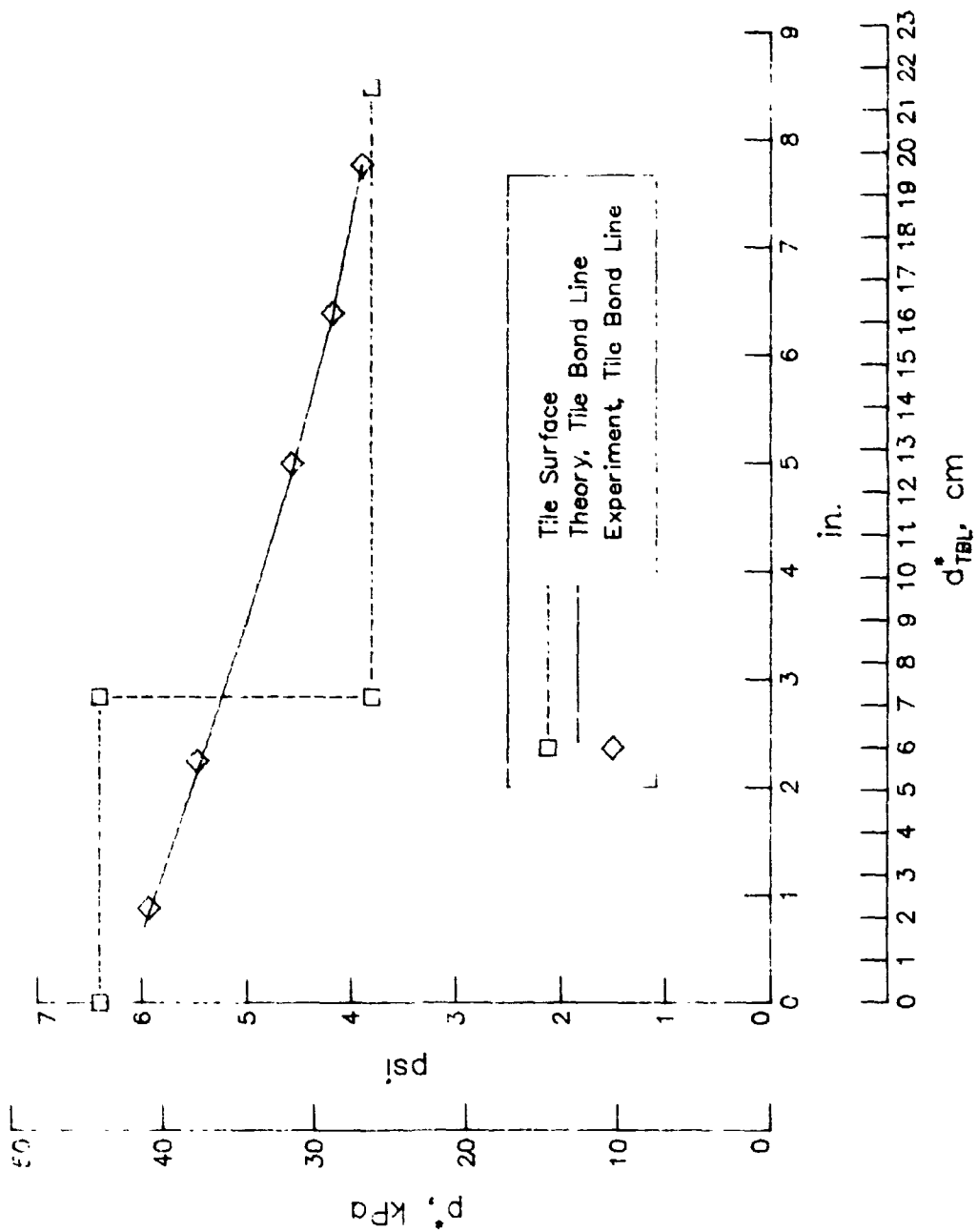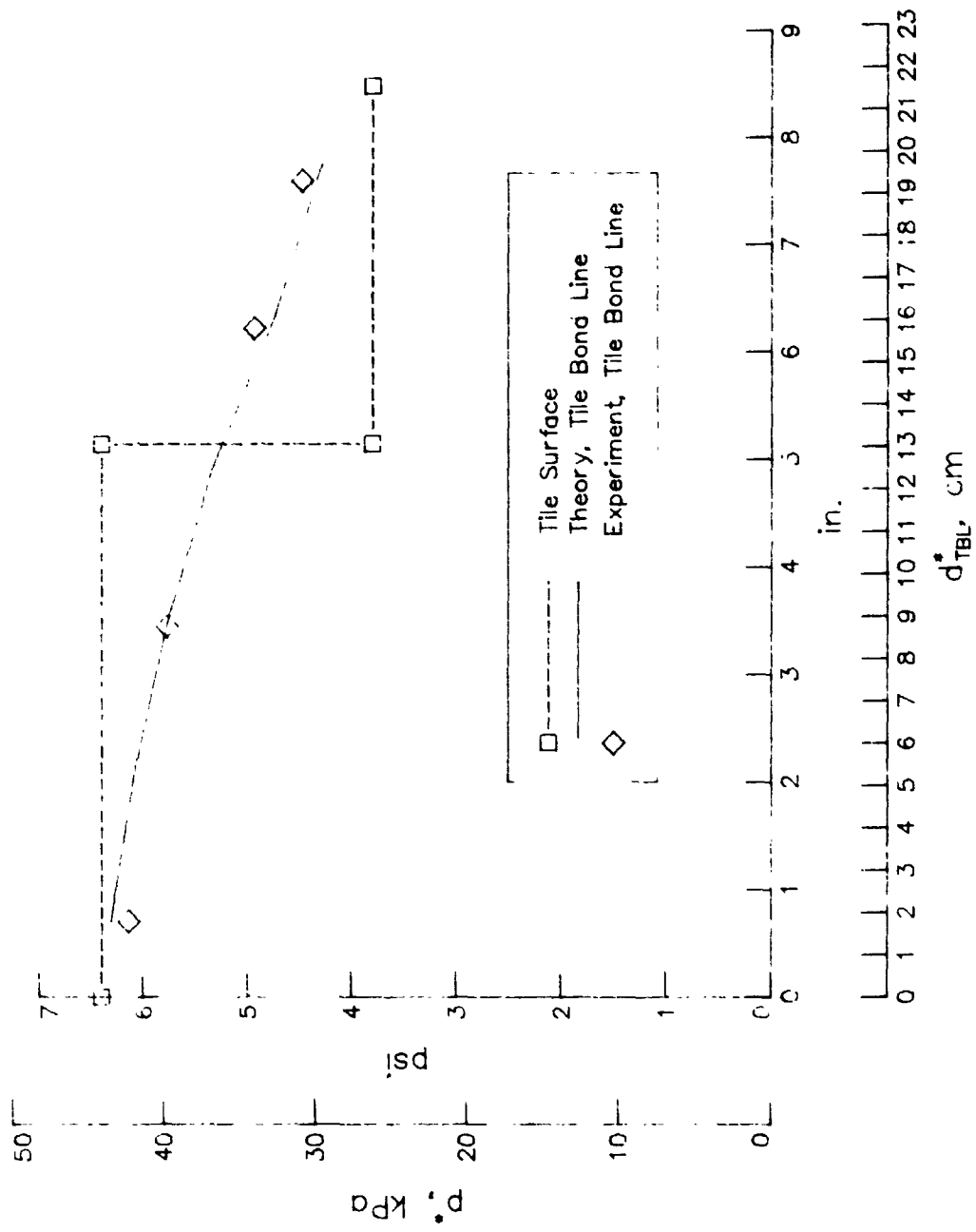Figure 10.- Continued.

(h) H = 4096.0.

Figure 10.- Concluded.

72

Figure 11.- Test setup for JSC simulated shock test.

Figure 12.- Comparison of JSC simulated shock test data and calculated pressure distributions at the tile bond line along the tile diagonal.

(a) Shock at 33%.

(b) Shock at 66%.

Figure 12.- Concluded.